

Scaling and Similarity of the Anisotropic Coherent Eddies in Near-Surface Atmospheric Turbulence

KHALED GHANNAM^a AND GABRIEL G. KATUL

Nicholas School of the Environment, Duke University, Durham, North Carolina

ELIE BOU-ZEID

Department of Civil and Environmental Engineering, Princeton University, Princeton, New Jersey

TOBIAS GERKEN

Department of Land Resources and Environmental Sciences, Montana State University, Bozeman, Montana

MARCELO CHAMECKI

Department of Atmospheric and Oceanic Sciences, University of California, Los Angeles, Los Angeles, California

(Manuscript received 19 August 2017, in final form 7 December 2017)

ABSTRACT

The low-wavenumber regime of the spectrum of turbulence commensurate with Townsend's "attached" eddies is investigated here for the near-neutral atmospheric surface layer (ASL) and the roughness sublayer (RSL) above vegetation canopies. The central thesis corroborates the significance of the imbalance between local production and dissipation of turbulence kinetic energy (TKE) and canopy shear in challenging the classical distance-from-the-wall scaling of canonical turbulent boundary layers. Using five experimental datasets (two vegetation canopy RSL flows, two ASL flows, and one open-channel experiment), this paper explores (i) the existence of a low-wavenumber k^{-1} scaling law in the (wind) velocity spectra or, equivalently, a logarithmic scaling $\ln(r)$ in the velocity structure functions; (ii) phenomenological aspects of these anisotropic scales as a departure from homogeneous and isotropic scales; and (iii) the collapse of experimental data when plotted with different similarity coordinates. The results show that the extent of the k^{-1} and/or $\ln(r)$ scaling for the longitudinal velocity is shorter in the RSL above canopies than in the ASL because of smaller scale separation in the former. Conversely, these scaling laws are absent in the vertical velocity spectra except at large distances from the wall. The analysis reveals that the statistics of the velocity differences Δu and Δw approach a Gaussian-like behavior at large scales and that these eddies are responsible for momentum/energy production corroborated by large positive (negative) excursions in Δu accompanied by negative (positive) ones in Δw . A length scale based on TKE dissipation collapses the velocity structure functions at different heights better than the inertial length scale.

1. Introduction

Besides their importance for predicting the exchange of matter and energy at the land–atmosphere interface, near-surface atmospheric flows offer a unique setting in the context of wall-bounded turbulence because of the large separation between inertial/outer (e.g., $\delta \sim 1000$ m)

and viscous ($\nu/u_* \sim 1$ mm) scales. In fact, neutrally stratified atmospheric surface layer (ASL) flows are often resorted to in pursuit of high-Reynolds number ($Re = u_*\delta/\nu$) experiments that are otherwise difficult to achieve in canonical turbulent boundary layers (e.g., Metzger and Klewicki 2001; Kunkel and Marusic 2006; Marusic et al. 2010). Here,¹ $u_* = \sqrt{\rho^{-1}\tau_s}$ is the friction

^a Current affiliation: Department of Civil and Environmental Engineering, Princeton University, Princeton, New Jersey.

Corresponding author: Khaled Ghannam, kghannam@princeton.edu

¹ Note that the terminology and nomenclature used by the atmospheric sciences community can be rather different from their experimental and theoretical fluid mechanics peers. Unless otherwise stated, meteorological notation and definitions are assumed here. Hutchins et al. (2012) provide a useful contrast on this issue that can extend substantially beyond a matter of notation.

velocity, δ is the atmospheric boundary layer (ABL) height (pipe radius or channel half-width in experimental fluids), $\tau_s \approx -\rho \overline{uw}$ is the shear stress at the surface, u and w are the turbulent fluctuations of the longitudinal (streamwise) and vertical (wall normal) velocity components around their corresponding time-averaged values U and W , ν and ρ are the kinematic viscosity and density of the fluid, and the overline or capital letters denote Reynolds (or time) averaging. Nevertheless, at least from an observational perspective, a one-to-one mapping of the scaling laws of velocity spectra and/or structure functions from wall turbulence to atmospheric flows has encountered mixed and at times contradictory findings. The notion that, away from the viscous subrange, the distance from the wall $z \gg \nu/u_*$ is the dominant similarity length scale for the intermediate (z scaling) region is particularly challenged in near-surface atmospheric flows. The latter argument is the focus of the work here.

A relatively consistent and systematic theory of high-Re wall-bounded turbulence seems to be currently endorssable, at least with regards to the mean flow and second-order turbulence statistics [recent reviews by Marusic et al. (2010) and Jiménez (2012)]. A central tenet of this theory is the existence of a self-similar inertial subrange (overlap or intermediate region) at distance z ($\nu/u_* \ll z \ll \delta$) normal to the wall/surface, in which the characteristic velocity and length scales are u_* and z (Townsend 1961). Both experimental and theoretical studies have supported logarithmic scaling laws in this sublayer for the mean $U/u_* = \kappa^{-1} \ln(z) + C_s$ (Prandtl 1925; von Kármán 1930), variance $\sigma_u^2 = \overline{u^2} = B_1 - A_1 \ln(z/\delta)$ (Townsend 1976; Marusic et al. 2013; Banerjee et al. 2015), and more recently all higher even-order moments $(\overline{u^{2p}})^{1/p} = B_p - A_p \ln(z/\delta)$ for $p \geq 1$ (Meneveau and Marusic 2013; Katul et al. 2016) of the longitudinal velocity. The constant A_1 (here in $\text{m}^2 \text{s}^{-2}$) is thought to be universal when made dimensionless such that $A_1/u_*^2 = 1.25$ (Stevens et al. 2014; de Silva et al. 2015), B_1 can depend on flow conditions, C_s is a wall/surface roughness constant, and $\kappa \approx 0.4$ is the von Kármán constant. Of particular interest here is the logarithmic scaling of σ_u^2 and the associated k^{-1} power law in the spectrum $E_{uu}(k)$ at low wavenumbers k (typically in the range $1/\delta < k < 1/z$). The spectrum $E_{uu}(k)$ is defined such that $\sigma_u^2 = \int_0^\infty E_{uu}(k) dk$, and when single-point time measurements are used, the wavenumber $k = 2\pi f/U$ corresponds to inverse longitudinal distance, inferred from frequency f (time) measurements of sonic or hot-wire anemometry by Taylor's frozen turbulence hypothesis (Taylor 1938). The two scaling laws follow from Townsend's model of attached eddies in the equilibrium/logarithmic region, where larger-than-inertial-scale coherent eddies of size $z < s < \delta$ are

attached to the wall/surface and sense its effects (Townsend 1961, 1976). Integrating $E_{uu}(k) \propto k^{-1}$ in the range $1/\delta \leq k \leq 1/z$ (attached eddies) recovers the $\sigma_u^2 \sim \ln(z/\delta)$ scaling, and hence, the two are equivalent (see also Banerjee and Katul 2013). It is worth noting that the inner (ν/u_*), inertial (z), and outer (δ) length scales are used here as limits indicative of eddy sizes and transitions in spectral scaling laws rather than exact cutoff length scales at which such transitions abruptly occur.

Perhaps the most popular explanation of the origin of the k^{-1} scaling in $E_{uu}(k)$ is the dimensional approach of Perry et al. (1986) based on Townsend's model of attached eddies (Townsend 1961, 1976), that is, the existence of large separation between the scales of motion or equivalently a sufficiently high Re. This k^{-1} scaling resides then between the very-large-scale motion (VLSM)² (Balakumar and Adrian 2007; Guala et al. 2011) ($E_{uu} \propto k^0$ for $k < 1/\delta$) and the finescale isotropic eddies that follow Kolmogorov's theory (Kolmogorov 1941, hereafter K41) [$E_{uu} \propto k^{-5/3}$ for $1/z \ll k \ll 1/\eta$, where $\eta = (\nu^3/\varepsilon)^{1/4}$ is the Kolmogorov microscale, and ε is the rate of viscous dissipation of turbulence kinetic energy (TKE) assumed equal to the mean rate of TKE transfer across scales]. Several other phenomenological (Nikora 1999) and theoretical (Tchen 1953; Katul et al. 2012) models also predicted or explained this k^{-1} scaling [Table 1 in Katul and Chu (1998) and Table 1 in Droinski et al. (2007) provide a survey of the literature]. Physically, at small vertical distances (close to the wall/surface) within the logarithmic region, the preferential suppression of the vertical velocity fluctuations w distorts large-scale coherent eddies of size $s > z$ in the streamwise direction, and turbulence becomes increasingly anisotropic as the wall/surface is approached (Davidson and Kroghstad 2014). These anisotropic/attached eddies are "active" in the shear production ($P = -\overline{uw} dU/dz$) of TKE, where the interaction between the momentum flux ($-\overline{uw}$) and the mean flow vorticity (dU/dz) mostly occurs. Hence, very close to the wall/surface, the spectrum of the longitudinal velocity is expected to exhibit three distinct ranges at scales much larger than η . In premultiplied form [i.e., $k E_{uu}(k)$], these are from small (high k) to large (low k) scales: (i) $k E_{uu}(k) \propto \varepsilon^{2/3} k^{-2/3}$ for $1/z \ll k \ll 1/\eta$. These isotropic eddies are denoted as "detached" here (no wall effects); (ii) $k E_{uu}(k) \propto k^0$ for $1/\delta < k < 1/z$ commensurate with the anisotropic production range. These

² VLSM is commonly referred to as inactive range/eddies because they do not contribute to stress and energy production. However, this range is part of energy transport, and we simply use VLSM to represent it. Perry and Abell (1977) called these non-universal motion because of the lack of self-similarity.

are denoted as “attached” eddies, and (iii) $k E_{uu}(k) \propto k^{+1}$ for $k < 1/\delta$ (VLSM).

At the experimental front, several studies on ASL flows reported a low-wavenumber k^{-1} regime in $E_{uu}(k)$ (e.g., Katul and Chu 1998; Högström et al. 2002; Drobinski et al. 2004). Both Högström et al. (2002) (their Fig. 5) and Drobinski et al. (2004) (their Figs. 6 and 7) show that the extent of the k^{-1} range decreases with increasing height above the surface, indicating that as the surface is approached in the logarithmic layer, the emergence of the anisotropic (k^{-1}) range comes at the expense of a narrower isotropic ($k^{-5/3}$) extent (Davidson and Krogstad 2014). Conversely, no k^{-1} scaling was detected in the Kansas (Kaimal et al. 1972) and some other ASL experiments (Busch and Panofsky 1968). It is also noticeable that Drobinski et al. (2004, 2007) observed an $E_{ww}(k) \propto k^{-1}$ scaling for the vertical velocity spectra around 30 m above the surface but not at lower heights in the near-neutral ASL. In turbulent boundary layer and pipe experiments, these mixed findings have also received attention (e.g., Del Álamo et al. 2004; Vallikivi et al. 2015, and references therein), mainly from a perspective of Re (scale separation) dependence.

The elusiveness of a clear k^{-1} scaling in $E_{uu}(k)$ has recently refocused the attention on its physical-space equivalent, the second-order structure function $D_{uu}(r) = [u(x+r) - u(x)]^2$ (definition in section 2) (Davidson et al. 2006; Davidson and Krogstad 2009, 2014; de Silva et al. 2015; Chung et al. 2015; Pan and Chamecki 2016; Chamecki et al. 2017). Here, where single-point time series measurements are used, $r = \tau U$ is the longitudinal separation distance, and $\tau = 1/f$ is the time separation. The functions $D_{uu}(r)$ and $E_{uu}(k)$ can be related by a simple Fourier transform (section 2), and hence, the k^{-1} power law is equivalent to a $\ln(r)$ scaling in $D_{uu}(r)$ in the production range, while the $k^{-5/3}$ in the finer-scale locally isotropic range is equivalent to the $r^{2/3}$ law that appeared in K41. Davidson et al. (2006) argued that the one-dimensional spectrum $E_{uu}(k)$ may not be the ideal tool for investigating and detecting the k^{-1} scaling because of large-scale (three dimensional) contamination in the one-dimensional spectra, an effect called aliasing. However, they were able to detect a logarithmic scaling in the structure function in both smooth- and rough-wall boundary layers in a wind tunnel experiment (Davidson and Krogstad 2014). The structure function also has the advantage of boundedness at large scales ($r \sim \delta$ or the integral length scale of the flow), where it flattens at $2\sigma_u^2$ (section 2). Beyond the existence of this logarithmic scaling, the analysis and experiments by Davidson and Krogstad (2014) showed that normalizing r by the dissipation-based length scale $l_\varepsilon = u_*^3/\varepsilon$ collapses experimental data at different heights

better than z , especially in the anisotropic production range. They attributed this deviation from the z scaling to the imbalance between the local production P and dissipation ε of TKE and proposed a $\ln(P/\varepsilon)$ correction to the $\ln(r/z)$ scaling. The dimensional analysis and LES experiments by Pan and Chamecki (2016) also showed that l_ε is the appropriate scale in the neutral-roughness sublayer of canopies (where $P/\varepsilon \approx 3$). Chamecki et al. (2017) later confirmed the superiority of l_ε over the z scaling in the unstable and stable ASL and found a k^{-1} regime under stable conditions.

Although the k^{-1} or $\ln(r)$ scaling laws and the associated transition/similarity length scales are still a subject of debate in canonical turbulent boundary layers, this paper identifies two aspects frequently encountered in atmospheric contexts where such issues remain inconclusive. These are (i) the existence of vegetation canopies where the flow in the roughness sublayer (RSL; defined here to extend from the canopy top until two to five canopy heights h) deviates appreciably from its ASL counterpart and (ii) the imbalance between local production and dissipation of TKE. While the two aspects may be related, where typically $P/\varepsilon \neq 1$ in the RSL of canopy flows, this imbalance is also not uncommon close to the surface in the ASL (e.g., Högström et al. 2002) and can be on the order of 20% (Charuchittipan and Wilson 2009). The work here uses several experiments to discuss the existence of this k^{-1} scaling in near-surface atmospheric flows, some of its phenomenological aspects, and the possible collapse of experimental data when plotted with inertial or some other similarity coordinates. The discussion also includes the scaling laws of the vertical velocity to characterize anisotropy. By using the notation “near surface,” we intend to contrast the near-neutral ASL above smooth and rough surfaces (≈ 1 –10 m above water bodies and short-grass fields), denoted as the eddy surface layer (ESL) by Hunt and Carloti (2001) and Drobinski et al. (2004), with flows in the immediate vicinity of tall roughness elements (directly above vegetation canopies) (Fig. 1).

Turbulent motion in the RSL above a dense canopy deviates from inertial-layer turbulence and is more analogous to mixing layers than to rough-wall boundary layers because of the strong shear at the canopy top (inflection point in the mean velocity U) (Raupach et al. 1996; Poggi et al. 2004). This mixing-layer analogy introduces an additional characteristic shear length scale [$l_s = U(dU/dz)^{-1}$] dictated by shear instabilities initiated at the canopy top (Fig. 1), besides the inertial length scale z . For canopy flows, z is defined to be above the zero-plane displacement height d_0 , where the latter is the height from the ground associated with the mean height of momentum absorption within the canopy.

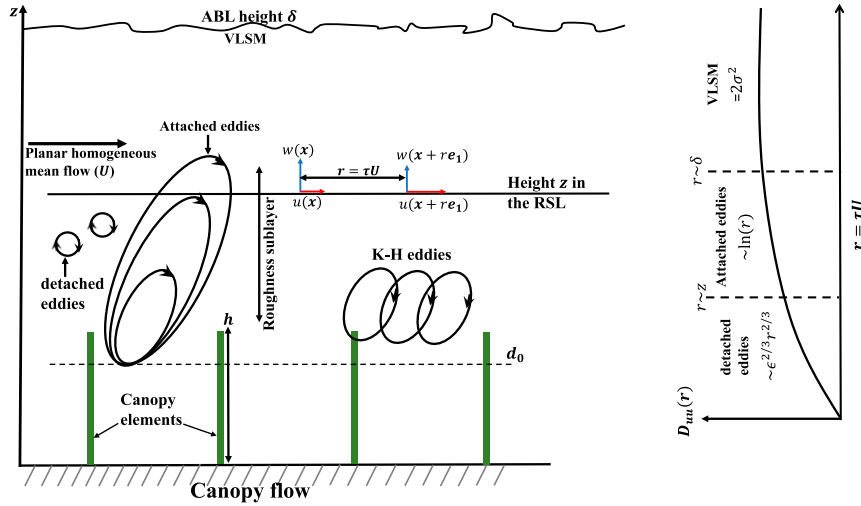


FIG. 1. Conceptual framework used to distinguish some features of canopy (roughness sublayer) from wall-bounded (e.g., surface layer) flows. At some height z above the canopy, eddies of size larger than z are considered attached to a displaced wall d_0 , while typically, much smaller eddies are detached (isotropic here) and follow K41 theory. The analysis is restricted to the mixing layer where Kelvin–Helmholtz (K-H) eddies are active. The velocity (u and w) structure functions are interpreted as functions of the longitudinal separation distance $r = \tau U$, where τ is time separation. Dimensions are not to scale, and h denotes canopy height. The height z and the direction and magnitude of the velocity components (red and blue arrows) are chosen arbitrarily for illustration.

Hence, with the assumption that u_* sets the inner boundary condition for all scales of motion and is indeed the characteristic velocity scale, the two aspects identified above reduce the discussion into an issue of length scales that challenge the classical z scaling. Figure 1 shows the conceptual framework used here to distinguish between RSL and ASL flows, where at some height $z \gg \nu/u_*$ above d_0 for canopies, eddies larger than z are attached to a displaced wall d_0 . Detached eddies that are much smaller than z are isotropic and follow the $r^{2/3}$ law.

To this end, five datasets (section 3) are used here to address the points raised earlier, namely, (i) the extent and height dependence of the $\ln(r)$ (or k^{-1}) scaling in the velocity structure functions (spectra), if any; (ii) some of its phenomenological aspects related to deviations from the characteristics of locally homogeneous and isotropic turbulence; and (iii) the collapse of experimental data at different heights using several dominant length scales. The experiments were conducted in the RSL of vegetation canopies (two experiments), close to the surface within the ASL (two experiments), and one lower-Re open-channel experiment for comparison with atmospheric flows. The work is limited to near-neutral flows, which are a common occurrence deep within the ABL above vegetation canopies or water bodies, as opposed to convective cases

where the ABL is dominated by large-scale thermal plumes (Ghannam et al. 2017; Salesky et al. 2017).

2. Definitions and theoretical framework

The coordinate system is defined such that x , y , and z form the longitudinal (streamwise), lateral (spanwise), and vertical (wall normal) directions, and the corresponding fluctuating velocity components are u , v , and w with Reynolds (time) averages U , V , and W . The mean flow is stationary $[\partial(\cdot)/\partial t = 0]$, planar homogeneous $[\partial(\cdot)/\partial x = \partial(\cdot)/\partial y = 0]$ for averaged quantities, and x is aligned with the mean flow U with no mean subsidence such that $V = W = 0$. With these assumptions, the second-order structure function for a velocity component α ($\alpha = u$ or w here) at some height z is given by

$$D_{\alpha\alpha}(r) = \overline{\Delta\alpha(r)\Delta\alpha(r)} = 2\sigma_\alpha^2[1 - \rho_{\alpha\alpha}(r)], \quad (1)$$

where $\Delta\alpha(r) = \alpha(\mathbf{x} + r\hat{\mathbf{e}}_x) - \alpha(\mathbf{x})$, \mathbf{x} is the position vector, $r = \tau U$ is the longitudinal spatial separation inferred from measured time separation (τ), $\hat{\mathbf{e}}_x$ is the unit vector in the x direction, and U is the local (height specific) mean velocity. Since spatial statistics are inferred from time measurements here, stationarity implies homogeneity, where all turbulence statistics, or otherwise

distributions of velocity differences, are independent of the time–space origin and are only functions of r . Both this assumption and planar homogeneity require $[\alpha(x+r)]^2 = [\alpha(x)]^2 = \sigma_\alpha^2$, and $\rho_{\alpha\alpha}(r) = \overline{\alpha(x+r)\alpha(x)}/\sigma_\alpha^2$ is the correlation coefficient that is the Fourier pair of $E_{\alpha\alpha}(k)$. The second-order structure function is a monotonically increasing function, ranging from $D_{\alpha\alpha}(0) = 0$ at $r=0$ [$\rho_{\alpha\alpha}(0) = 1$] to $D_{\alpha\alpha}(L_\alpha) = 2\sigma_\alpha^2$ at $r = L_\alpha$ [$\rho_{\alpha\alpha}(L_\alpha) = 0$], where L_α is the integral length scale of the velocity component α . Note that $D_{\alpha\alpha}(r)$ is a measure of the cumulative contribution of eddies of size r or less to the energy (per unit mass) σ_α^2 , and $r dD_{\alpha\alpha}(r)/dr$ is roughly the energy contained in eddies of size r (Townsend 1976; Davidson and Krogstad 2014). The interest here is in the scaling laws of $D_{\alpha\alpha}(r)$ at different heights z in the ASL and RSL and the transition/similarity length scales associated with these laws. In light of the earlier discussion, the scaling laws (see Fig. 1) in the isotropic (detached eddies), active/production (attached eddies), and VLSM ranges are, respectively,

$$D_{uu}(r) = C\varepsilon^{2/3}r^{2/3}, \quad \eta \ll r \ll l, \quad (2)$$

$$D_{uu}(r) = B + A \ln\left(\frac{r}{l}\right), \quad l \ll r \ll \delta, \quad \text{and} \quad (3)$$

$$D_{uu}(r) = 2\sigma_u^2 = 2\left[B_1 - A_1 \ln\left(\frac{z}{\delta}\right)\right], \quad r \sim L_u \sim \delta, \quad (4)$$

where $C \approx 2.2$ is the Kolmogorov constant, A and B are additional constants, and l is some characteristic length scale. Since the structure function is commonly plotted against $\ln(r)$, the constant A will be referred to as the slope in Eq. (3). The dimensional analysis by Davidson and Krogstad (2014), Pan and Chamecki (2016), and Chamecki et al. (2017) showed that $l \propto l_\varepsilon$ in Eq. (3) is the correct similarity length scale for the production range. Equations (3) and (4) follow from each other at scales $r \sim L_u \sim \delta$ with $l \sim z$, and by matching the two scaling laws, one obtains $A/u_*^2 = 2A_1/u_*^2 \approx 2.5$ (e.g., Chung et al. 2015; de Silva et al. 2015). The logarithmic scaling in $D_{uu}(r)$ also follows from the assumption that the kinetic energy of the space-filling attached eddies scales with the momentum flux, such that $r dD_{uu}(r)/dr \sim u_*^2$, from which Eq. (3) follows accordingly. Note that Eq. (2) can be written as

$$\frac{D_{uu}(r)}{u_*^2} = C \left(\frac{r}{l_\varepsilon}\right)^{2/3}, \quad (5)$$

and by the universality of C , the dissipation length scale $l_\varepsilon(z) = u_*^3/\varepsilon(z)$ collapses the inertial subrange (isotropic detached eddies) of the normalized structure function at different heights in the constant flux region ($d\overline{uw}/dz \approx 0$). For a logarithmic $U(z)$, $P = -\overline{uw} dU/dz \approx u_*^3/\kappa z$, and a

local balance between P and ε implies that $l_P \propto l_\varepsilon \propto \kappa z$, where $l_P = u_*^3/P$ is the production length scale (Pan and Chamecki 2016; Chamecki et al. 2017). The latter arguments are the basis for the classical z scaling in the intermediate region of wall-bounded shear flows, and both are challenged here where turbulent flows in the RSL deviate from inertial-layer flows and $P \neq \varepsilon$. Nevertheless, if $dU/dz = u_*/\kappa z$ is a good approximation (more so for near-neutral ASL than RSL flows), then the production length scale $l_P \approx \kappa z$, the dissipation length scale $l_\varepsilon = (P/\varepsilon)\kappa z$, and the shear length scale $l_s = (U/u_*)\kappa z$. Equation (3) can be written with $l = l_\varepsilon$ as

$$\begin{aligned} D_{uu}(r) &= B + A \ln\left(\frac{r}{l_\varepsilon}\right) \\ &= B - A \ln\left(\frac{P}{\varepsilon}\right) + A \ln\left(\frac{r}{\kappa z}\right), \end{aligned} \quad (6)$$

or with $l = l_s$,

$$\begin{aligned} D_{uu}(r) &= B + A \ln\left(\frac{r}{l_s}\right) \\ &= B + A \ln\left(\frac{u_*}{U}\right) + A \ln\left(\frac{r}{\kappa z}\right), \end{aligned} \quad (7)$$

respectively. In other words, besides the typical inertial scaling $\ln(r/\kappa z)$, l_ε accounts for the imbalance between P and ε with the term $\ln(P/\varepsilon)$ [this correction appeared in Davidson and Krogstad (2009) and Davidson and Krogstad (2014)], while l_s accounts for the effects of drag (u_*/U) at the canopy top.

To connect these various length scales (κz , l_ε , l_P , and l_s) to turbulent eddies and scaling laws of velocity structure functions, the phenomenology of the attached eddies [Eq. (3)] as a departure from the well-studied locally homogeneous and isotropic turbulence is also of interest here. The latter finescale eddies ($r \ll l$) belong to the stages of Richardson's cascade where energy is neither produced nor dissipated but simply transported from larger eddies ($r > l$) that extract energy from the mean flow down to the viscous scales ($r \sim \eta$). In this respect, the probability density functions $G[\Delta\alpha^+(r)]$ ($\alpha = u$ or w) of the velocity differences are examined in the locally isotropic ($r \ll l$) and anisotropic ($r > l$) ranges (plus sign indicates velocity normalization by u_*). The skewness $\text{Sk}[\Delta\alpha^+(r)] = (\Delta\alpha^+)^3/[(\Delta\alpha^+)^2]^{3/2}$ and excess flatness factors $F[\Delta\alpha^+(r)] = (\Delta\alpha^+)^4/[(\Delta\alpha^+)^2]^2 - 3$ (excess is defined as above the Gaussian value of 3) of these distributions are functions of the longitudinal separation distance r and, hence, are indicative of the transition between locally isotropic (non Gaussian) and anisotropic (close to Gaussian) scales. Note that

TABLE 1. Site and experimental characteristics. Note that the columns correspond to z : approximate measurement height; h : average canopy height; f : sampling frequency; time: run/block time length; runs: number of blocks analyzed; and the ranges of u_* , U , and $|L_o|$ across the runs. See section 3 for further details. Range of values of u_* and U across all the runs calculated at the lowest measurement height ($z/h \approx 1$ for canopies).

Expt	z (m)	h (m)	f (Hz)	Time (min)	Runs	u_* (m s ⁻¹)	U (m s ⁻¹)	$ L_o $ (m)
AMA	35, 40.25, 48.3	35	20	30	24	0.2–0.7	1–2.6	450–15 000
MAI	2.1, 2.8, 3.5	2.1	20	30	15	0.43–0.51	1.56–1.95	67–12 000
LAKE	1.65, 2.3, 2.95, 3.6	—	20	30	63	0.12–0.57	1.2–10.6	90–3000
AHATS	1.5, 3.3, 4.2, 5.5, 7, 8	—	60	36.4	15	0.2–0.4	2.42–5	170–15 000
OC	0.006, 0.01	—	100	1.365	1	0.009	0.2	—

$\text{Sk}[\Delta u^+(r)]$ for the longitudinal velocity component is equivalent to the structure skewness $S(r)$ defined as (Obukhov 1949; Monin and Yaglom 1975)

$$S(r) = \frac{D_{uuu}(r)}{[D_{uu}(r)]^{3/2}}, \quad (8)$$

where $D_{uuu}(r) = \overline{[u(x+r) - u(x)]^3}$ is the third-order structure function. Obukhov (1949) hypothesized that $S(r)$ is constant in locally homogeneous and isotropic flows and proposed this constant-skewness assumption as a closure to the Kármán–Howarth–Kolmogorov equation (von Kármán and Howarth 1938; K41)

$$D_{uuu}(r) - 6\nu \frac{dD_{uu}(r)}{dr} = -\frac{4}{5}\varepsilon r, \quad (9)$$

that relates the second- and third-order structure functions in the universal (inertial and viscous) isotropic range. At scales $\eta \ll r \ll l$ within this range, the effects of viscosity [second term in Eq. (9)] are negligible, and Kolmogorov’s “4/5” law is recovered

$$D_{uuu}(r) = -\frac{4}{5}\varepsilon r, \quad (10)$$

such that, using Eqs. (2), (8), and (10), the skewness $S(r)$ in the inertial/isotropic range is roughly constant (Katul et al. 1997, 2015)

$$S(\eta \ll r \ll l) \approx -0.22, \quad (11)$$

subject to some experimental uncertainty and Re effects. Deviations from these relatively established results for the inertial subrange are used to examine the phenomenology of the anisotropic range. Experiments, data, and methods of estimating the TKE dissipation rate ε and the dominant length scales are now presented.

3. Data and methods

This section reviews the main features of the five experiments (published datasets) used in the analysis. Site

characteristics and flow conditions are summarized in Table 1, and length-scale estimations are presented here. The two canopy experiments have an order-of-magnitude difference in canopy height h and are intended to examine the effects of canopy morphology and distance from the wall on the anisotropic range of the velocity structure functions. The work is limited to several heights above the canopy in the RSL. The ASL experiments were conducted above a lake and a short-grass field within 10 m above the surface, whereas the open-channel flow is used as a reference canonical turbulent boundary layer. In RSL and ASL cases, the flow is near neutral with atmospheric stability parameter $|z/L_o| < 0.05$, where L_o is the Obukhov length and z is the highest measurement height.

a. Experiments

The five experiments are as follows:

- Amazonian canopy (AMA): The experiment was part of the Observations and Modeling of the Green Ocean Amazon (GoAmazon) project, and its details are documented in Fuentes et al. (2016), Freire et al. (2017), and Gerken et al. (2018). The data were collected during a field campaign at the Cuieiras Biological Reserve, located 60 km north-northwest of the city of Manaus, Brazil, between March 2014 and January 2015 at a 50-m-tall tower surrounded by a dense primary forest. The average canopy height at the measurement site is $h \approx 35$ m, with leaf area index estimated to be between 5.7 and 7.3 m² m⁻². High-frequency time series of the three wind velocity components within and immediately above the canopy were continuously measured by nine triaxial sonic anemometers (model CSAT3, Campbell Scientific, Logan, Utah) between March 2014 and January 2015. The measurement frequency is 20 Hz, and approximate measurement heights are $z/h = 0.2, 0.39, 0.52, 0.63, 0.7, 0.9, 1, 1.15$, and 1.38. Measurements within the canopy are used here only for estimating the displacement height d_0 , while the structure function analysis is restricted to heights

$z/h = 1, 1.15$, and 1.38 within the RSL. A total of 24 data runs/blocks (30 min each) were analyzed (see Table 1).

- **Maize canopy (MAI):** This experiment was conducted in a large flat field planted with maize near Mahomet, Illinois, between June and July 2011 (Gleicher et al. 2014; Chamecki 2013; Pan et al. 2016). The average canopy height is $h \approx 2.1$ m, and the leaf area index during the measurement period is $\approx 3.3 \text{ m}^2 \text{ m}^{-2}$. The three wind velocity components were sampled using five triaxial sonic anemometers (model CSAT3, Campbell Scientific) at a 20-Hz frequency. The approximate measurement heights are $z/h = 0.33, 0.67, 1, 1.33$, and 1.67 , and similar to the AMA canopy, the analysis is restricted to $z/h \geq 1$. Pan and Chamecki (2016) used a 7.5-h turbulence time series ($u_* = 0.51 \text{ m s}^{-1}$) from measurements at this site. Here, this 7.5-h data block is split into 15 runs (30 min each) to minimize possible effects of nonstationarity. These runs are used as replicate realizations (see Table 1).
- **Lake Geneva (LAKE):** The measurements were part of the Lake–Atmosphere Turbulent Exchange (LATEX) field campaign over Lake Geneva, Switzerland (Vercauteren et al. 2008; Bou-Zeid et al. 2008; Li et al. 2016) and were collected on a 10-m-high tower, 100 m away from the shore of the lake. The campaign lasted from mid-August until late October 2006. Four sonic anemometers (CSAT3, Campbell Scientific) were deployed at heights of 1.65, 2.30, 2.95, and 3.60 m above the water surface to sample the three-component wind field at 20 Hz. The four measurement heights are used here and a total of 63 runs (30 min each) are analyzed (Table 1).
- **Advection Horizontal Array Turbulence Study (AHATS):** The experiment took place near Kettleman City, California, during the period from 25 July to 16 August 2008 (UCAR–NCAR Earth Observing Laboratory 1990; Salesky and Chamecki 2012). The field site was surrounded by short-grass stubble and was predominantly horizontally homogeneous and level. Data from the AHATS profile tower, consisting of six CSAT3 sonic anemometers (Campbell Scientific) mounted at heights $z \approx 1.5, 3.30, 4.2, 5.5, 7$, and 8 m are used here. The sampling frequency was 60 Hz, and a total of 15 runs (36.4 min each) are analyzed (Table 1).
- **Open channel (OC):** The details of this experiment are documented in Katul and Chu (1998) and Katul et al. (2012). Briefly, the experiment was conducted at Cornell University in a 20-m-long, 1.0-m-wide, and 0.8-m-deep open-channel tilting flume with a smooth stainless steel bed. The channel slope was set at 0.0001 mm^{-1} , resulting in $h_w = 10.3$ cm of water depth.

The longitudinal and vertical velocity components were measured using a two-dimensional split-film boundary layer probe (TSI 1287W model). The sampling frequency was 100 Hz, and the measurement period lasted for 1.365 min at measurement heights $z = 0.1, 0.2, 0.3, 0.4, 0.6$, and 1 cm. Only the highest measurement levels $z = 0.6$ and 1 cm corresponding to $z^+ \approx 55$ and 92 are used here, where $z^+ = zu_*/\nu$ and $u_* = 0.9 \text{ cm s}^{-1}$. The mean velocity is $U \approx 0.2 \text{ m s}^{-1}$, and only one run is available.

The multiple runs for each experiment were selected on the basis that (i) the momentum flux \overline{uw} was relatively constant with height (to within 10%), and hence, it is assumed that the analysis is within the constant flux region, and (ii) the corresponding turbulence intensity $I_u = \sigma_u/U$ is less than 0.25 across these runs, a common practice to minimize the effects of using Taylor's frozen turbulence hypothesis. By assuming that all wavenumbers (eddies) are convected with the same velocity U , the longitudinal spatial separation $r = \tau U$ and wavenumber $k = 2\pi f/U$ are then inferred from the time separation τ (or f) and U . The corrections to the use of Taylor's hypothesis suggested by Wyngaard and Clifford (1977) and Hsieh and Katul (1997) in the inertial subrange are also implemented (discussed in the next subsection). We also note that the uncertainty in estimating u_* from sonic anemometers and its slight change with height are difficult to avoid in ASL experiments. Nonetheless, in all our parameter estimations and data normalization, local (height specific) values of u_* are used throughout.

In what follows, for presentation and brevity purposes, we show results only from one individual run at each site (with multiple heights each), and statistics across all runs are presented whenever applicable. The profiles of the mean flow statistics (normalized by appropriate powers of u_*) for this sample run are shown in Fig. 2. The height z is normalized by canopy height h in the top row of Fig. 2 for canopy experiments and by z_h for the ASL and open channel experiments (bottom row), where z_h is the highest measurement location ($z_h = 3.6$ m for LAKE, 8 m for AHATS, and 1 cm for OC; Table 1). A distinctive feature of canopy flows is the strong shear at the canopy top, manifesting itself by a much smaller U/u_* (or equivalently higher turbulence intensity) in the RSL (Fig. 2a) compared to the ASL (Fig. 2e). All higher-order moments in the RSL (Figs. 2b–d) follow typical profiles of plant canopies [see a review by, e.g., Finnigan (2000)] and approach their ASL counterpart as z/h increases. The mixed third-order moments \overline{wuu} and \overline{wuu} in Figs. 2d and 2h, or more precisely their gradients, are responsible for nonlocal

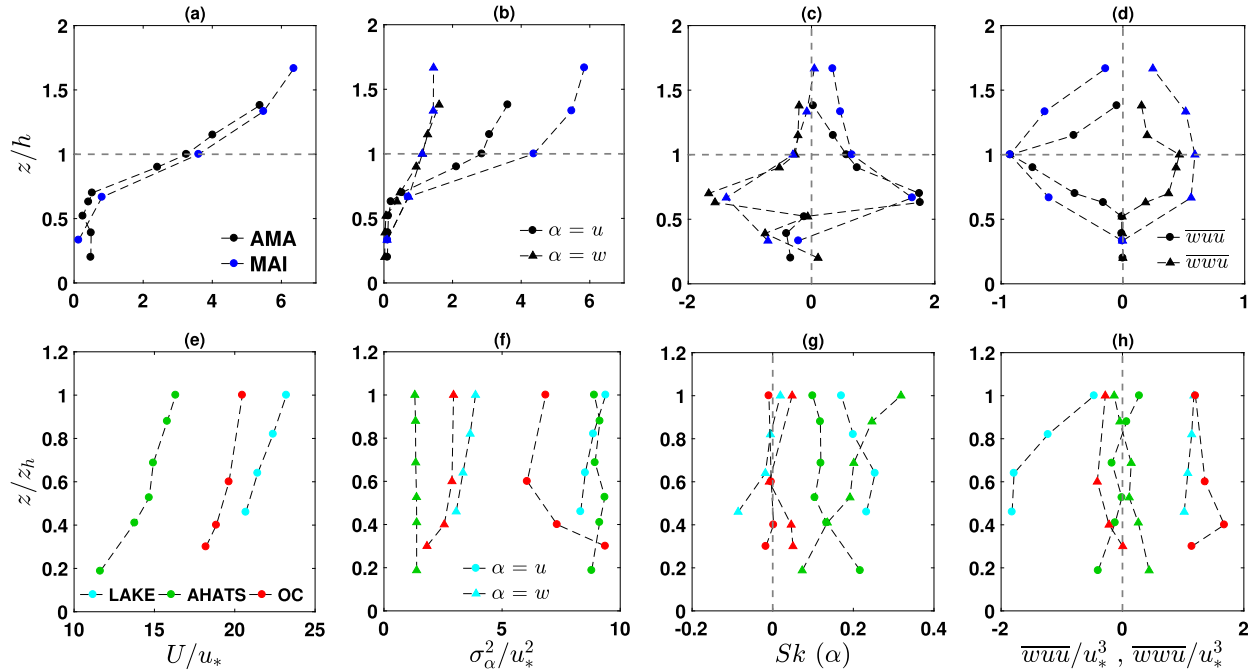


FIG. 2. Dimensionless profiles of mean-flow statistics for a select experimental run at each site/experiment (see Table 1) for (a),(e) mean longitudinal velocity component, (b),(f) velocity variances, (c),(g) velocity skewness, and (d),(h) mixed third-order velocity moments. The normalizing scales are the friction velocity u_* , canopy height h , and highest measurement location z_h . (a)–(d) Amazonian (AMA; black; $h = 35$ m) and maize (MAI; blue; $h = 2.1$ m) canopy experiments. (e)–(h) Smooth- and rough-wall experiments for open channel (OC; red; $z_h = 1$ cm), AHATS (green; $z_h = 8$ m), and Lake Geneva (LAKE; cyan; $z_h = 3.6$ m). The velocity components u and w are represented by the circle and triangle symbols, respectively. Note that full profiles are shown for canopy experiments but subsequent analysis is restricted to flow above the canopy ($z/h \geq 1$).

transport of TKE and velocity variances. These moments are significant deep within the RSL and the ASL and decrease with increasing height z , indicating that $P/\varepsilon \neq 1$ very close to the wall/surface.

b. Dissipation and length-scale estimation

From Wyngaard and Clifford (1977) and Hsieh and Katul (1997), the structure functions inferred from Taylor's hypothesis are corrected in the inertial subrange for finite I_u , such that Eq. (2) becomes $D_{uu}(r) = C[F_u(I_u)]\varepsilon^{2/3}r^{2/3}$, where $F_u(I_u) = 1 + (11/9)I_u^2$ and $I_u = \sigma_u/U$ is the turbulence intensity. A similar correction for $D_{ww}(r)$ with $F_w(I_u) = 1 + (11/36)I_u^2$ is also used. Since $I_u < 0.25$ for all experiments, $F_u(I_u)$ across all sites and runs is less than 1.08, and hence, the corrections are reasonably small, well within the uncertainty in the value of $C \approx 2.2$. The inertial subrange is identified from the compensated second-order structure function $r^{-2/3}D_{uu}(r)$, which exhibits a relatively flat or constant range equal to $C\varepsilon^{2/3}$ [see Eq. (2)], typically for $0.3 < r < 2$ m in the experiments here (depending on the measurement height and sampling frequency). After Chamecki and Dias (2004) and Chamecki et al. (2017), the TKE dissipation rate ε is then estimated by averaging

over this range, which extended for less than half a decade close to the surface in the ASL and RSL to one to two decades at higher z . Estimating ε from the vertical velocity structure function $D_{ww}(r)$ in a similar manner did not result in any significant differences. However, estimates from $D_{uuu}(r) = -(4/5)\varepsilon r$ in the inertial subrange were unreliable because of the noisy nature of high-order moments computed from measurements. Chamecki et al. (2017), who also used the AHATS data, showed that ε estimates from $D_{uuu}(r)$ were approximately 30% smaller (on average) than the ones from $D_{uu}(r)$. In the rest of the paper, ε values determined from the inertial subrange of $D_{uu}(r)$ are used.

To estimate the displacement height d_0 for the AMA and MAI canopies, the momentum flux \overline{uw} within the canopy ($0 < z \leq h$) was fitted to a fourth-order polynomial in z , and the drag force $F_d(z) = d\overline{uw}/dz$ is determined (the estimate is not sensitive to third- or fifth-order polynomial fits). The height d_0 is then calculated from

$$d_0 = \frac{\int_0^h z F_d(z) dz}{\int_0^h F_d(z) dz}, \quad (12)$$

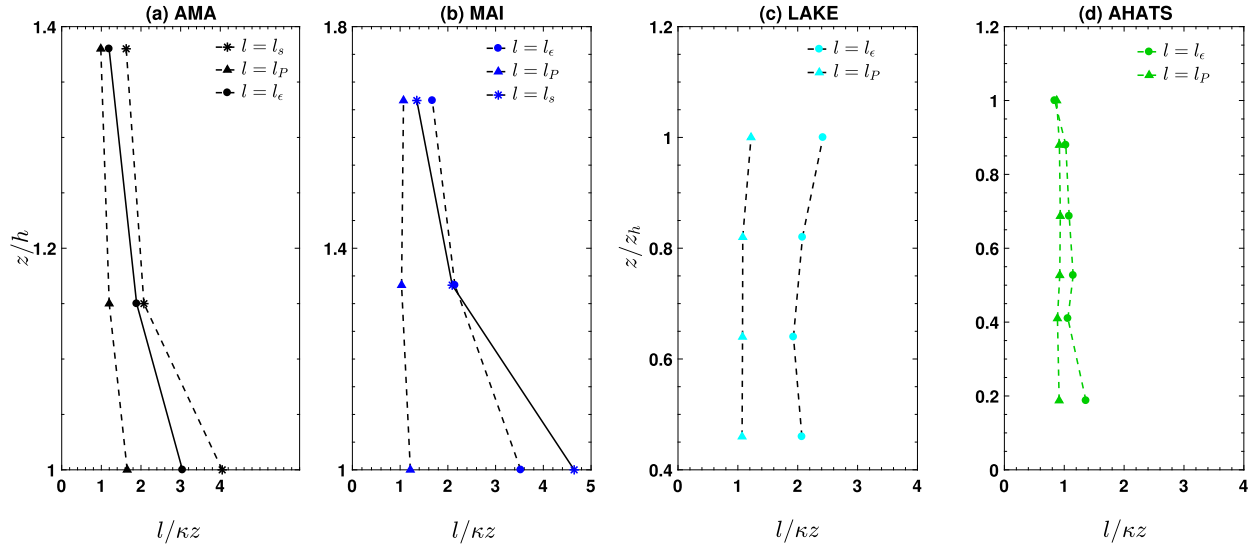


FIG. 3. Profiles of the ratio ($l/\kappa z$) of several length scales l to the inertial length scale κz against (a),(b) z/h and (c),(d) z/z_h for the experimental run in Fig. 2. (a),(b) For canopies, κz is to be interpreted as the height above the zero-plane displacement.

as the mean height associated with momentum absorption. The range for the AMA canopy is $0.73 \leq d_0/h \leq 0.79$ ($h \approx 35$ m) across the 24 runs and for the MAI canopy is $0.69 \leq d_0/h \leq 0.74$ ($h \approx 2.1$ m) across the 15 runs. This indicates that the distance from the displaced wall d_0 for the AMA canopy is between ≈ 10 and 24 m at the three measurement heights (see Table 1), while the range is ≈ 0.6 –2 m for the MAI canopy. Similarly, the mean velocity (U) profile was fitted to a second-order polynomial in $\ln(z)$ for all experiments, from which the production and shear (only for canopies) length scales are estimated as $l_P = u_*^3/P$ and $l_s = U/(dU/dz)$, where $P = -\overline{uw}dU/dz$ is used. For canopies, the mean velocity log-polynomial fits are limited to $z/h \geq 0.9$, where three data points are available in this range (see Table 1). The dissipation length scale $l_\varepsilon = u_*^3/\varepsilon$ is calculated using the ε estimates from $D_{uu}(r)$ as discussed earlier. These z -dependent length scales, normalized by the inertial length scale κz , are shown in Fig. 3 for the data run presented above (Fig. 2). The ratio $l_P/\kappa z$ (filled-triangle symbols) is indicative of deviations from a logarithmic mean velocity profile, and except for the OC (Fig. 3e), where the highest measurement height is $z^+ \approx 99$ ($z^+ = zu_*/\nu$), this ratio is close to unity at all heights for the other experiments (Figs. 3a–d). In contrast, $l_\varepsilon/\kappa z$, which is then approximately $l_\varepsilon/l_P = P/\varepsilon$, deviates appreciably from unity deep within the RSL (less so for the ASL) and approaches κz at higher heights. The shear length scale l_s follows l_ε closely in the RSL. This finding was also noted in the LES runs of Pan and Chamecki (2016) for the MAI canopy, although l_s estimated from the data here exceeded l_ε at the canopy top.

These length scales are used in subsequent sections to explore the phenomenology and the collapse of the large anisotropic scales.

Before presenting the results, it is worth noting that when l_ε is estimated from the inertial subrange of the longitudinal velocity structure function, it is bound to collapse $D_{uu}(r)$ at small r . This collapse of data is not necessarily the case for larger scales in $D_{uu}(r)$ and/or $D_{ww}(r)$ that are of interest here.

4. Results and discussion

a. Scaling laws of velocity structure functions and spectra

Since the $\ln(r)$ and/or k^{-1} (k^0 in premultiplied form) scaling laws can be elusive when using experimental data, Fig. 4 shows both the normalized structure function D_{uu}/u_*^2 and premultiplied spectra kE_{uu}/u_*^2 at all measurement heights from each experiment. These are plotted against $r/\kappa z$ and kz on a log–log scale and multiplied by an arbitrary constant (vertical shift) for clarity. The $r^{2/3}$ (Fig. 4a) and $k^{-2/3}$ (Fig. 4b) power laws expected in the isotropic range are shown as solid gray lines to depict the extent of this subrange and deviations therefrom. Note that these are not data fits and are only used here to indicate the commencement of the logarithmic (or k^{-1}) scaling laws. Nevertheless, the logarithmic fits in Fig. 4a (dashed gray lines) are not forced to start at these scales (i.e., where D_{uu} deviates from the $r^{2/3}$ scaling) but rather fitted within a range at larger r (between 3 – $8\kappa z$ and $20\kappa z$) and the resulting linear [in $\ln(r/\kappa z)$] fits are extended over a wider range. The

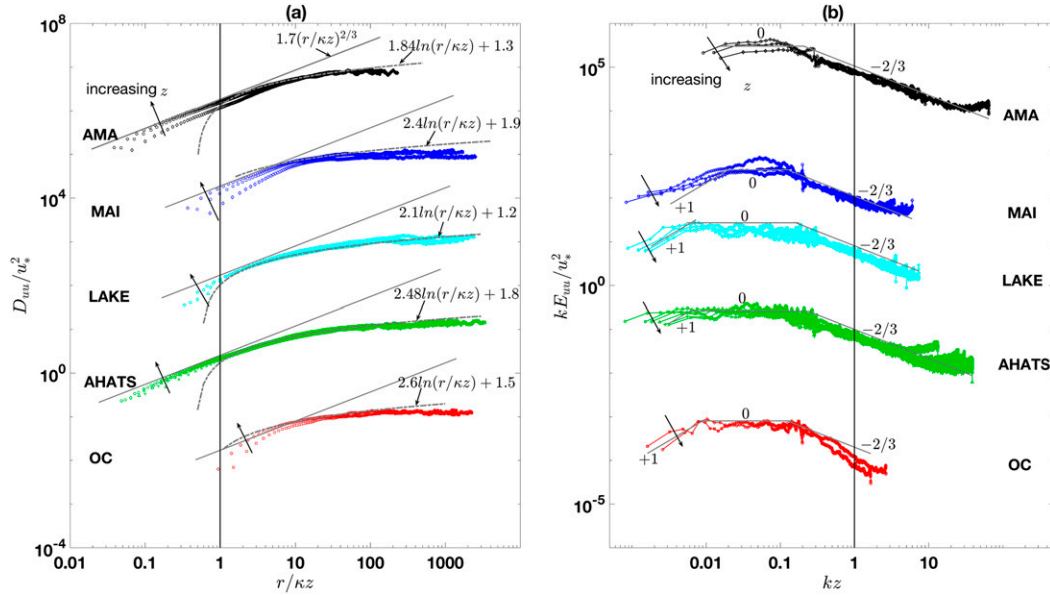


FIG. 4. (a) Normalized structure function (D_{uu}/u_*^2) of the longitudinal velocity component against $r/\kappa z$ at each site/experiment for all measurement heights (see Table 1). Note that r is the longitudinal separation distance and z is the distance from the surface/wall (or zero-plane displacement for canopies). The solid and dashed gray lines denote the $r^{2/3}$ (inertial range) and logarithmic law/fits (production range), respectively. (b) The corresponding normalized and premultiplied spectra (kE_{uu}/u_*^2) of the longitudinal velocity component plotted against kz , where k is the longitudinal wavenumber. The solid gray lines denote the k^{+1} (nonuniversal/VLSM range), k^0 (production range), and $k^{-2/3}$ (inertial range) power laws. All plots are shifted vertically by two decades (except AHATS data) for clarity.

slope A [Eq. (3)] of the fits to the anisotropic range in the measured structure function (Fig. 4a) compares well with the values ($A \approx 2.5$) estimated from matching arguments (e.g., de Silva et al. 2015), as introduced earlier in section 2. Both Figs. 4a and 4b show that this anisotropic range commences at scales larger than z (around $1.2z$ – $5z$ depending on the experiment), as opposed to the classical z scaling that typically assumes $kz = 1$ (shown as vertical black line in Fig. 4b) sets such a transition [e.g., the experiments by Katul and Chu (1998)]. These are inferred from the approximate start of this range, roughly $3 < r/\kappa z < 8$ (Fig. 4a) and $0.2 < kz < 0.3$ (Fig. 4b), with no significant differences between RSL and ASL experiments. However, canopy cases (AMA and MAI) show a shorter k^0 [or $\ln(r)$] range, extending for less than half a decade in both E_{uu} and D_{uu} . This is due to the fact that the integral length scale of the longitudinal velocity component L_u is much smaller in the RSL than in the ASL, typically within $h < L_u < 3h$ in the former (Finnigan 2000) and $L_u \sim \delta$ in the latter.

Conversely, similar analysis for the vertical velocity (D_{ww} and E_{ww}) at the same measurement heights shows a much smaller scale separation (Fig. 5). Although the premultiplied spectra for the AMA, LAKE,

and AHATS experiments exhibit a short (less than a decade) k^0 range, the slope of the logarithmic fits to the structure function D_{ww} (Fig. 5) is smaller ($A < 1$), indicating that D_{ww} attains $2\sigma_w^2$ rapidly with increasing scale. For these sites, $kz \approx 1$ seems to set the end of the $k^{-2/3}$ scaling, while this isotropic range extends to scales larger than z ($kz < 1$) in the MAI and OC experiments. Overall, after repeating such an exercise by examining $D_{\alpha\alpha}$ and $E_{\alpha\alpha}$ ($\alpha = u$ and w) for all data runs and all experimental sites, we note that using either approach (from an experimental view) to hunt for the $\ln(r)$ or k^{-1} scaling laws is elusive, and here, we contrast both means in pursuit of that. In particular, the structure function is commonly plotted against $\ln(r)$, and hence, fitting a linear trend [Eq. (3)] over a short range of scales to find the $\ln(r)$ law can be misleading. Theoretically, the separation of scales between the integral length scales L_α and the upper limit of the inertial subrange, be it $\approx z$ or some other limit/range l , is indicative of the crossover between the $r^{2/3}$ and $2\sigma_\alpha^2$ regimes. This scale separation is height dependent and increases with increasing z (always close to the surface within the RSL or ASL). Figure 6 depicts this argument, where both D_{uu} (red lines) and D_{ww} (blue lines) are plotted at all available measurement heights for each experiment, with the

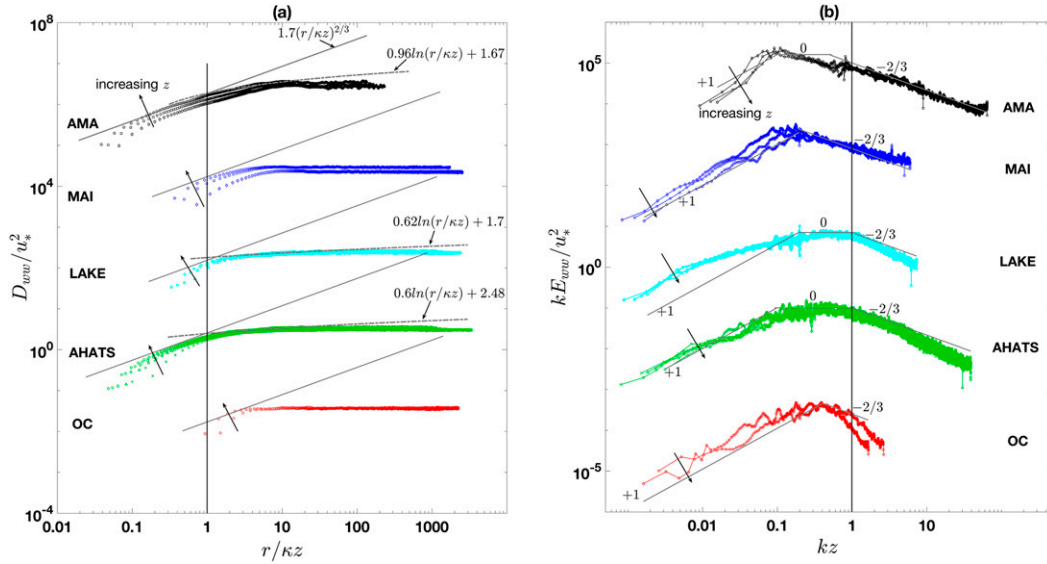


FIG. 5. As in Fig. 4, but for the vertical velocity component.

lowest height at the bottom. In canopy cases (Figs. 6a and 6b), deviations from the $r^{2/3}$ (gray lines) power law in both D_{uu} and D_{ww} have a short extent before reaching the integral length scales L_u and L_w (shown as short vertical lines). On the other hand, the ASL and channel experiments (Figs. 6c–e) show an extensive overlap region for D_{uu} but not D_{ww} . Both integral length scales,

calculated empirically from the correlation function $\rho_{\alpha\alpha}(r)$, exhibit a minor change with height within the RSL and ASL.

In addition to the existence and height dependence of the logarithmic scaling in D_{uu} , the slope A in Eq. (3) is also of interest. This slope has dimensions of energy density, where in the production range $r dD_{uu}(r)/dr = A$,

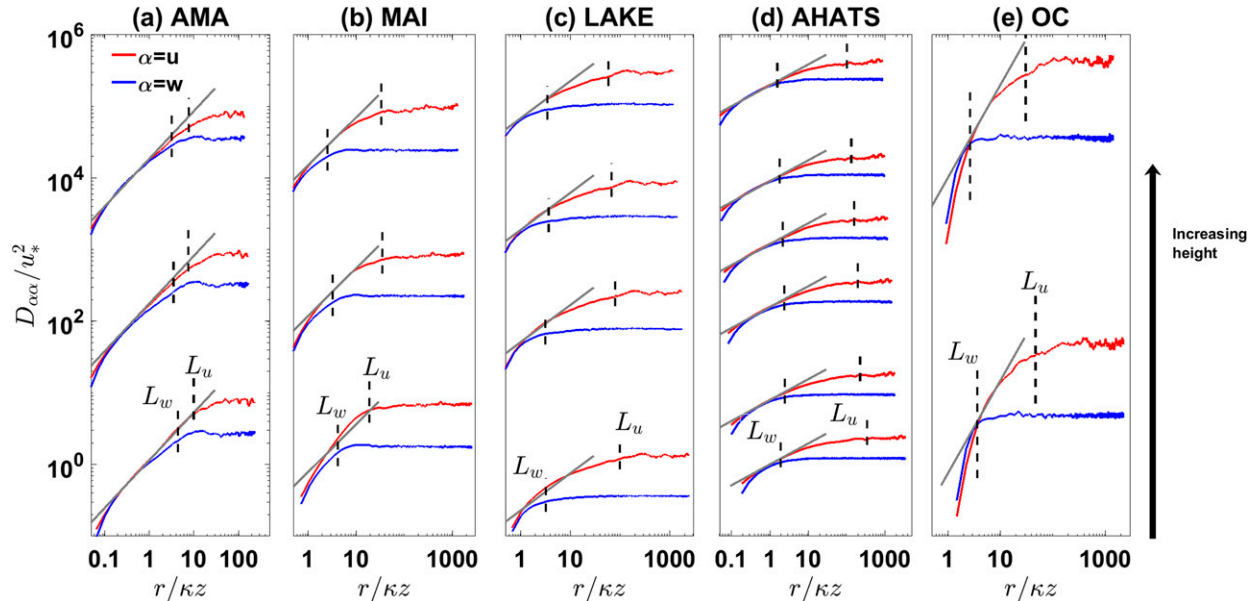


FIG. 6. Normalized structure functions ($D_{\alpha\alpha}/u_*^2$) with $\alpha = u$ (red) and $\alpha = w$ (blue) plotted against $r/\kappa z$ at all measurement heights for (a) AMA (three heights), (b) MAI (three heights), (c) LAKE (four heights), (d) AHATS (six heights), and (e) OC (two heights). The separation distances $r = L_u$ (integral length scale for u component) and $r = L_w$ (integral length scale for w component) are shown at each height with a vertical dashed black line. The solid gray lines denote the $r^{2/3}$ (inertial range) power law. All plots are shifted vertically with the lowest measurement height at the bottom.

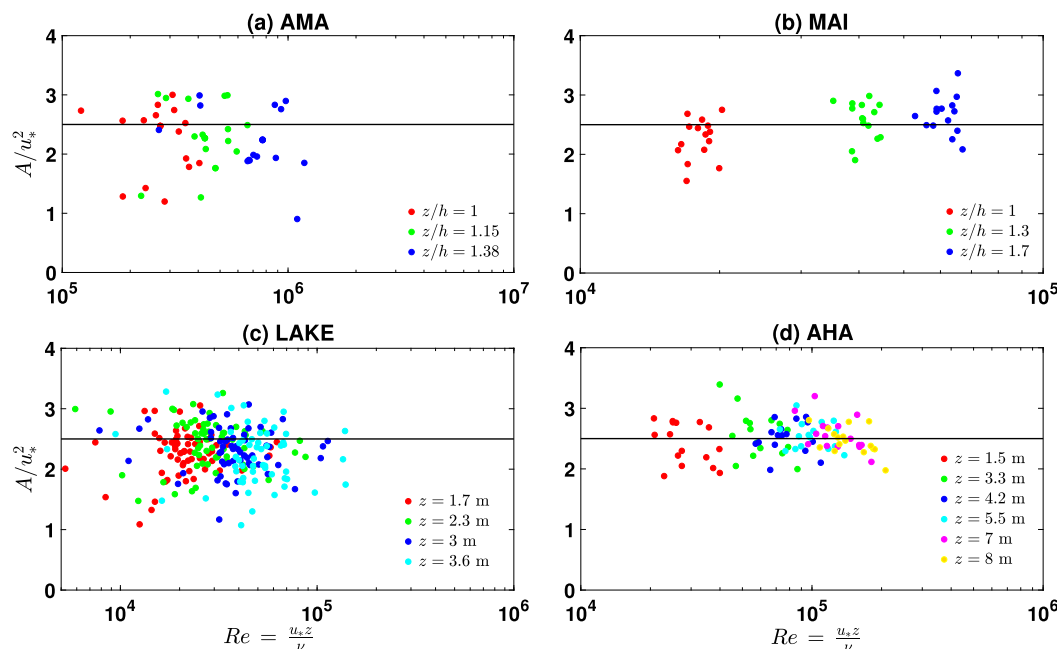


FIG. 7. Dimensionless slope (A/u_*^2) of the logarithmic scaling (production range) in $D_{uu}(r)$ estimated from fits for all available data runs at each site, plotted against the local $Re = u_* z / \nu$. Each color denotes a height z or z/h for canopies (see legend), and each filled circle symbol represents a single data block. The black horizontal line is the universal value $A/u_*^2 = 2.5$.

hence implying that the energy distribution across the attached eddies is uniform. Since the logarithmic scaling in Eq. (3) can be derived from the argument that in the production range $r dD_{uu}(r)/dr \sim u_*^2$, it is argued that the dimensionless slope A/u_*^2 is therefore universal (≈ 2.5). Figure 7 shows the value of A/u_*^2 obtained by fitting a logarithmic scaling to $D_{uu}(r)$ at each measurement height and each data run for the experiments here, plotted against the local Reynolds number $Re = u_* z / \nu$ (where z is above d_0 for canopies). Figure 7 depicts that, on average, A/u_*^2 is close to the value 2.5 (black horizontal line) at all heights/ Re with a tendency for a slight increase with height in the RSL. The scatter in the values of A/u_*^2 may be due to small uncertainties in estimations of TKE dissipation rate and/or the use of Taylor's hypothesis, which may in turn affect the existence and extent of a logarithmic scaling in $D_{uu}(r)$ (Pan and Chamecki 2016). To disentangle the origins of this scale separation and transitions between isotropic and anisotropic scales, some phenomenological aspects of the turbulence scales are discussed next.

b. Phenomenology of the anisotropic range

The age (or extent) of the anisotropic coherent structures that follow the logarithmic scaling explored earlier is the main theme of this section. As such, the probability density functions (pdfs) of the velocity

differences $\Delta u^+(r)$ and $\Delta w^+(r)$ are shown in Fig. 8 at two separation scales: $r \ll l_e$ indicative of the detached isotropic eddies and $r \gg l_e$ to sample anisotropic eddies. These are for the highest measurement location at each site as earlier. Both $\Delta u^+(r)$ and $\Delta w^+(r)$ have a zero mean, and the separation scales are chosen for illustration, where the length scale l_e is used since it is typically larger than z ($P/\varepsilon > 1$); hence, $r \gg l_e$ is in the production range. At small scales, the pdfs $G[\Delta u^+(r \ll l_e)]$ and $G[\Delta w^+(r \ll l_e)]$ (Figs. 8a and 8c) exhibit heavier tails than at larger scales (Figs. 8b and 8d) for all sites. The tails of small-scale turbulence are known to decay much slower than Gaussian (Anselmetti et al. 1984; Sreenivasan and Antonia 1997) and approach a Gaussian distribution at larger scales. While the excursions/tails of Δu^+ and Δw^+ appear smaller for canopies at $r \ll l_e$ than in the ASL (Figs. 8a and 8c), these are simply due to a higher u_* ; that is, canopy flows in fact experience larger excursions in velocity differences at small scales, especially in the longitudinal velocity component u . The importance of these individual pdfs here is that they encode the statistical moments of turbulence in $\Delta u^+(r)$ and $\Delta w^+(r)$. For instance, the second moment (variance) of each of these distributions is the value of the structure functions D_{uu} and D_{ww} at the scale r , which was explored earlier in Figs. 4 and 5, such that the variances $[\Delta u^+(r)]^2$ and $[\Delta w^+(r)]^2$ at some large r are the

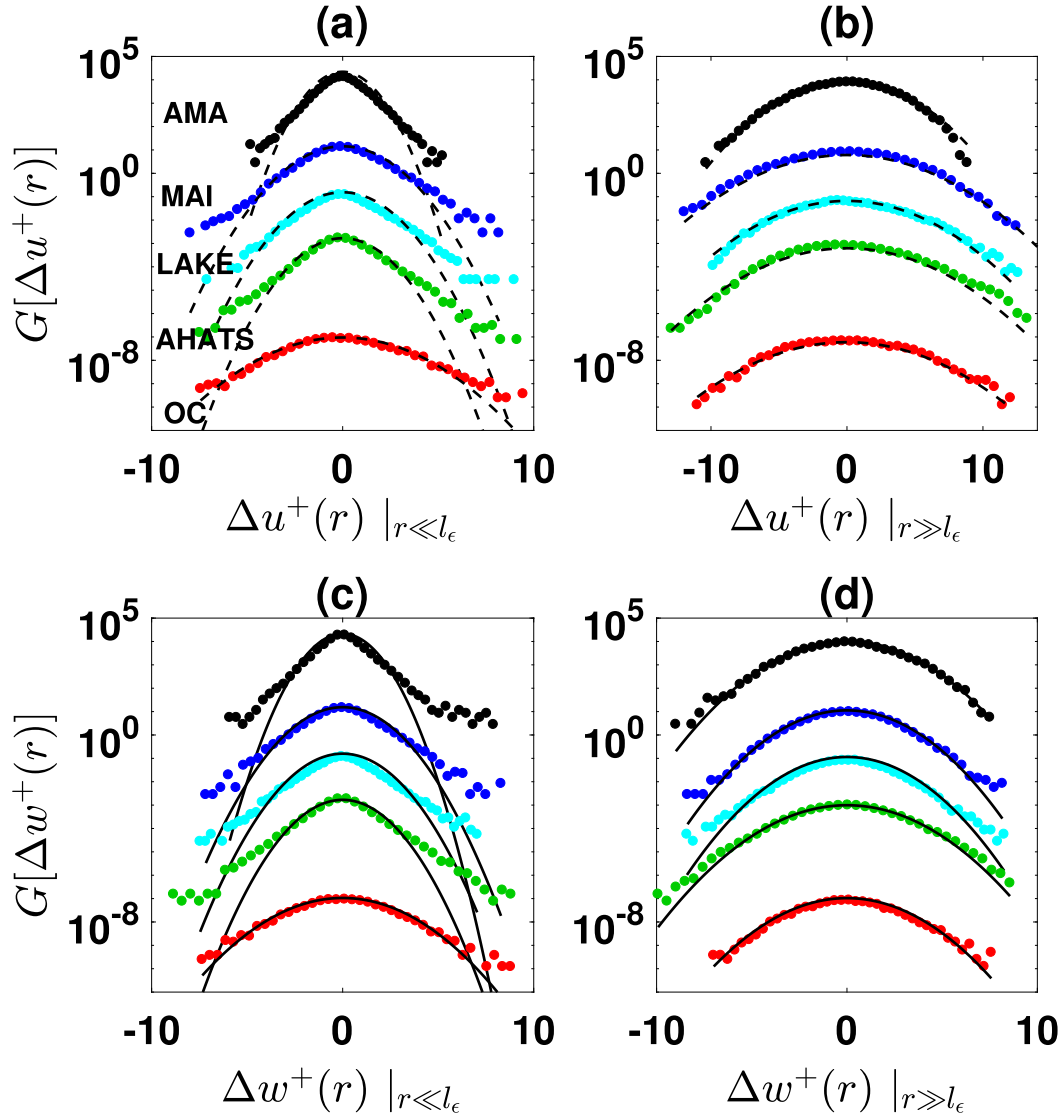


FIG. 8. The pdfs of the normalized (by u_*) velocity differences: (a),(b) $\Delta u^+(r)$ and (c),(d) $\Delta w^+(r)$ at two selected separation distances. In (a) and (c), the separation distance is $r \ll l_\epsilon$ (isotropic range), and in (b) and (d), $r \gg l_\epsilon$ (anisotropic range). A Gaussian pdf with zero mean and a variance equal to that of the data is shown by black lines. Only the highest measurement height at each site is presented, and all plots are shifted vertically for clarity.

cumulative contribution from all the corresponding distributions at smaller separation distances. To examine how fast the pdfs approach a Gaussian distribution, the skewness $\text{Sk}[\Delta \alpha^+(r)]$ and excess flatness factors $F[\Delta \alpha^+(r)]$ ($\alpha = u$ and w) of these distributions are plotted against $r/\kappa z$ in Fig. 9. Both Sk and F have a decreasing trend with increasing scale r , indicating that the pdf of velocity differences approaches a Gaussian-like distribution at large r . Also, these moments generally decay slower (with r) for the longitudinal $[\Delta u^+(r)]$ than the vertical $[\Delta w^+(r)]$ velocity differences because of the larger scale separation in u compared to w . It is

interesting to note that the flatness factors F for both velocity components collapse with κz in all experiments and approach zero (equivalent to the Gaussian value 3) around $10 \kappa z$. The AMA and AHATS experiments have the largest scale separation between l_ϵ (vertical lines in Fig. 9) or κz and the scale r at which the moments approach values close to a Gaussian distribution. These experiments have the largest distance from the wall ($z = 24$ m above d_0 for AMA and $z = 8$ m for AHATS; Table 1) compared to the other experiments, and note that both exhibited a limited k^{-1} scaling in E_{ww} (Fig. 5). In such contexts, no significant differences on scale

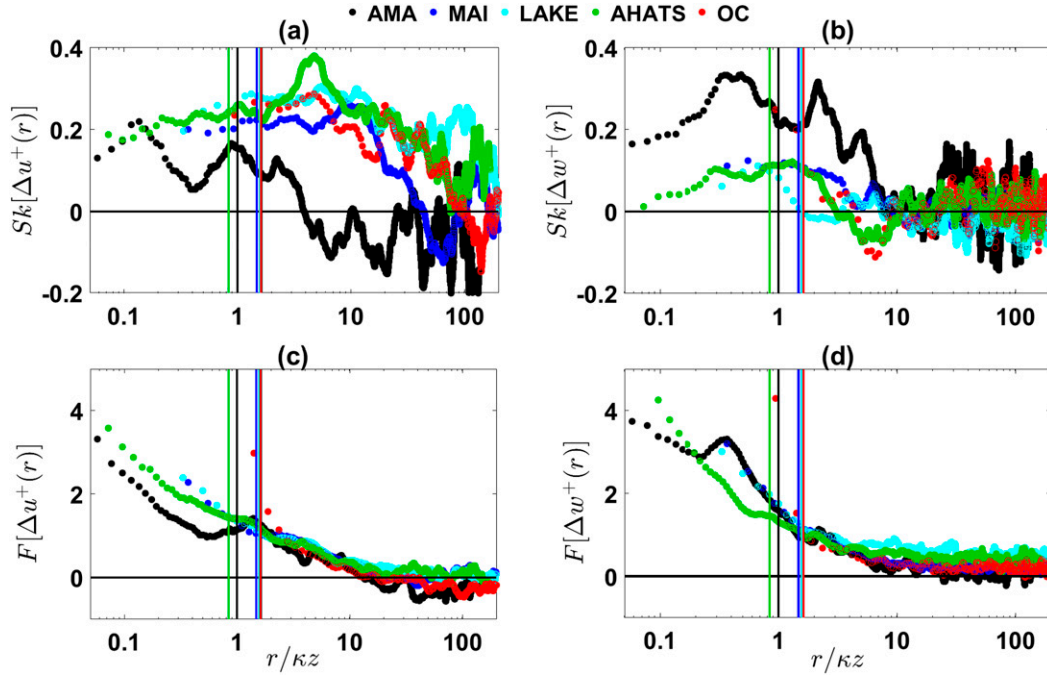


FIG. 9. (a),(b) Skewness (Sk) and (c),(d) excess (above Gaussian value of 3) flatness factor F of the distributions of velocity differences as a function of $r/\kappa z$. Different sites are represented by colors consistent with Fig. 8. The vertical lines correspond to $r = l_e$ at each site.

separation between the RSL and ASL seem noticeable, but rather, the distance from the wall emerges as a more important factor.

Besides the individual pdfs that characterize the scalewise contribution to the diagonal elements (σ_u^2 and σ_w^2) of the stress tensor through D_{uu} and D_{ww} , another important attribute is the stress/energy production by the scales of motion. The anisotropic coherent eddies are known to be the scales where turbulence (momentum flux $-\overline{uw} = u_*^2$) interacts with the mean flow dU/dz to produce energy/variances. As such, the mixed second-order structure function $D_{uw}/u_*^2 = \overline{\Delta u^+(x+r)\Delta w^+(x)}$ that involves lagged (in r) cross correlations between the velocity components is now explored. Upon expansion, this normalized structure function can be written as

$$\begin{aligned} \frac{D_{uw}(r)}{u_*^2} &= 2 - \frac{\overline{u(x)w(x+r)}}{u_*^2} - \frac{\overline{u(x+r)w(x)}}{u_*^2} \\ &\approx 2 - 2 \frac{\overline{u(x)w(x+r)}}{u_*^2}, \end{aligned} \quad (13)$$

where it is assumed that $\overline{u(x+r)w(x+r)} = \overline{u(x)w(x)}$ by planar homogeneity, and the first term on the right-hand side is $2\overline{u(x)w(x)}/u_*^2 = 2$. Also, after examination of the data from all experiments and at all available heights, the assumption $\overline{u(x)w(x+r)} \approx \overline{u(x+r)w(x)}$ appears

reasonable here (data not shown). Hence, at very small scales (e.g., $r \ll l_e$ or z ; isotropic range), the velocity components u and w are well correlated and $\overline{u(x)w(x+r)} \approx u_*^2$, indicating no contribution to the momentum flux $\overline{u(x)w(x)}$ from these small eddies. As r increases and the velocity components decorrelate [i.e., the second term in Eq. (13) decreases to zero], the larger-scale eddies cumulatively contribute to the momentum flux. This argument is investigated here by sampling the isotropic and anisotropic eddies in an analogous manner to the usual quadrant analysis of (u, w) fluctuations, typically used for characterizing ejection–sweep events. Figure 10 shows such a scalewise analysis for $\Delta u^+(r)$ and $\Delta w^+(r)$. The scatterplots of these quantities against each other in the isotropic ($r \ll l_e$; Fig. 10b) and anisotropic ($r \gg l_e$; Fig. 10c) scales suggest that at small separation distances r , the contributions from the four quadrants in Fig. 10b to the product $\overline{\Delta u^+ \Delta w^+}$ cancel each other, while at $r \gg l_e$, the second ($\Delta u^+ < 0, \Delta w^+ > 0$) and fourth ($\Delta u^+ > 0, \Delta w^+ < 0$) quadrants dominate the contribution to the negative momentum flux. This picture is consistent across all experiments. Figure 10a shows the joint pdfs of $(\Delta u^+, \Delta w^+)$ for the scatterplots in Figs. 10b and 10c, with the filled/colored contours representing the isotropic scales in Fig. 10b and the gray contours corresponding with the energy-producing eddies in Fig. 10c.

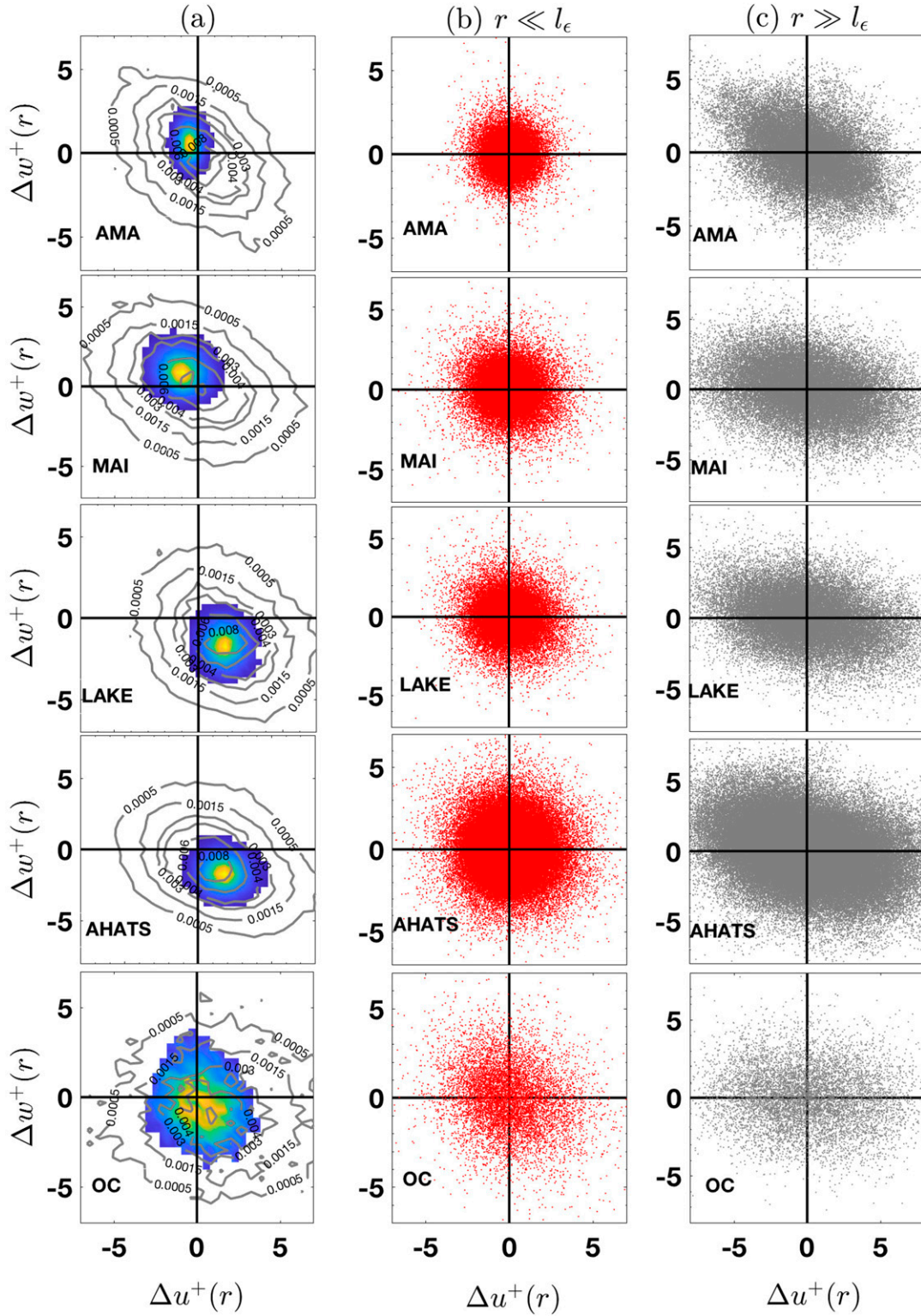


FIG. 10. (a) Joint pdfs of $\Delta u^+(r)$ and $\Delta w^+(r)$ in the isotropic ($r \ll l_\epsilon$, colored contours) and anisotropic ($r \gg l_\epsilon$, gray contours) eddies at the highest measurement level for each experiment. The joint pdfs in (a) are calculated based on the scatterplot of $\Delta u^+(r)$ and $\Delta w^+(r)$ in (b) isotropic ($r \ll l_\epsilon$) and (c) anisotropic ($r \gg l_\epsilon$) range.

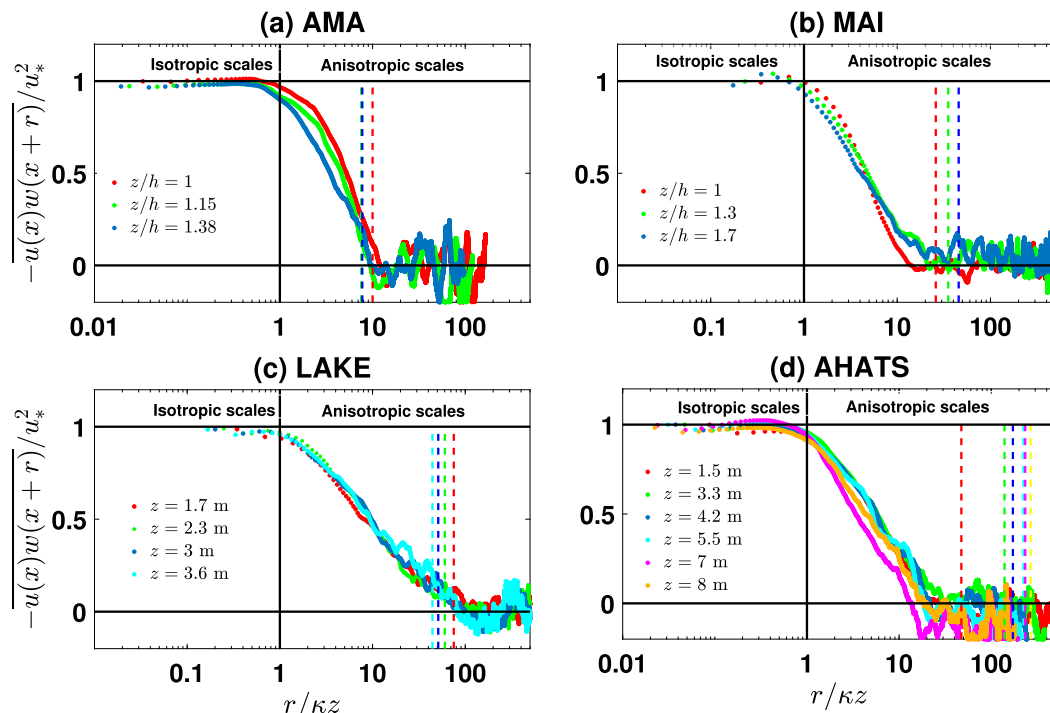


FIG. 11. Lagged cross correlation $\overline{u(x)w(x+r)}$ (note the negative sign) in Eq. (13) normalized by u_*^2 at all heights for each experiment. The dashed vertical lines correspond to the integral length scale L_u at each height, with their colors matching the legend for heights.

The analysis in Fig. 10c (or gray contours in Fig. 10a) shows that within the large-scale coherent eddies, it is the simultaneous occurrence of strong excursions/gradients in Δu^+ , be these positive or negative, accompanied with strong excursions in Δw^+ of the opposite sign, that lead to shear production. By examining the second ($\Delta u^+ < 0, \Delta w^+ > 0$) and fourth ($\Delta u^+ > 0, \Delta w^+ < 0$) quadrants in Fig. 10c, it appears that the two mechanisms, namely, large negative Δu^+ excursions accompanied by large positive Δw^+ ones (second quadrant; analogous to ejection events), or the opposite (fourth quadrant; analogous to sweeping events) are equally likely to produce momentum.

As opposed to the usual quadrant analysis of the ejection-sweep cycle that does not account for scalewise contributions, the analysis here samples all eddy sizes and reflects on their role in shear/energy production. For instance, the lagged cross correlation $\overline{u(x)w(x+r)}/u_*^2$ [second term in Eq. (13)] is shown in Fig. 11 for all experiments and at all heights. The OC experiment behaves similarly to ASL experiments and is no longer included in the analysis here for brevity. At small scales ($\approx r < \kappa z$ in Fig. 11), the velocity components $u(x)$ and $w(x+r)$ are well correlated and $\overline{u(x)w(x+r)} \approx \overline{u(x)w(x)} = u_*^2$, while as r increases, larger eddies accumulate momentum until $r \sim L_u$

(shown as vertical dashed lines in Fig. 11). Within the anisotropic range, it is evident that shear production is stronger at the larger-scale coherent motion and decreases as eddies cascade to smaller scales until isotropy is attained and no more shear is produced. It is worth noting that these shear-producing eddies extend to a wider range (about two decades) in the ASL (Figs. 11c and 11d) than in the RSL (about one decade) (Figs. 11a and 11b), where L_u is smaller in the latter.

The last two components of the phenomenology of the anisotropic range relate the structure function $D_{uu}(r)$ to its third-order counterpart $D_{uuu}(r)$ through the structure skewness $S(r)$ [Eq. (8)] and to the vertical velocity structure function $D_{ww}(r)$. Both are well studied in the isotropic range where $S(r) \approx -0.22$ and $D_{uuu}/D_{ww} \approx 3/4$ (ratio of the Kolmogorov constants for D_{uu} and D_{ww} in the universal isotropic range). Figure 12 shows the negative of the skewness $S(r)$ as inferred from Eq. (8) plotted against $r/\kappa z$ for all the experiments. The length scales l_e, l_s , and L_u for the highest measurement location are also shown. The value $S(r) \approx -0.22$ seems a satisfactory approximation at small scales, particularly for the ASL experiments (Figs. 12c and 12d), while it is slightly lower in the RSL (Figs. 12a and 12b). Deviations from this value occur at or before $r \approx \kappa z$ and decay faster in the RSL above canopies than in the ASL. There is no

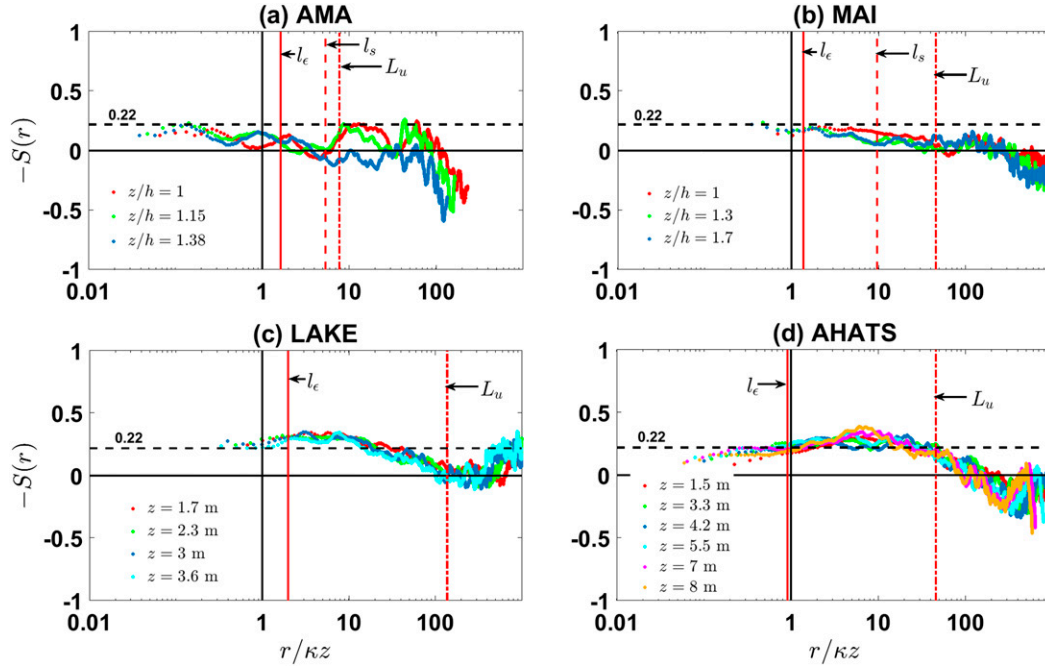


FIG. 12. The negative of the structure skewness in Eq. (8) for the atmospheric experiments plotted against $r/\kappa z$ at each measurement height on a log-linear scale. The length scales l_ϵ , l_s , and L_u are shown as solid, dashed, and dash-dotted red lines, respectively. These are from the highest measurement height in each experiment for illustration. The value $S(r) \approx -0.22$ [see Eq. (11)] expected in the isotropic range is shown as a black dashed horizontal line in each panel.

strong height dependence in $S(r)$, although it is noticeable that the inertial length scale κz collapses $S(r)$ at different heights in the ASL but not in the RSL. The negative values of $S(r)$ in both the isotropic (≈ -0.22) and anisotropic ranges indicate that $D_{uuu}(r) = [u(x+r) - u(x)]^3 < 0$, and hence, at these scales, the magnitude of both negative and positive excursions in the longitudinal velocity fluctuations tend to decrease. Similar analysis for D_{uu}/D_{ww} (Fig. 13) shows that this ratio is close to the expected “3/4” constant in the isotropic range and departs fast from this constant around $r \approx \kappa z$. At those larger scales, if D_{uu} exhibits a logarithmic scaling while D_{ww} attains $2\sigma_w^2$, the ratio D_{uu}/D_{ww} should also show a logarithmic scaling in r . This seems to be the case for all experiments except for AMA, which exhibits a logarithmic scaling in D_{ww} . The ratio D_{uu}/D_{ww} approaches the constant $(\sigma_u/\sigma_w)^2$ (calculated from the data and plotted as dashed horizontal lines in Fig. 13) at the very large scales, indicating a reasonable convergence of the scalewise fluctuations to bulk turbulence statistics.

c. Similarity length scales

Figure 14 shows the collapse of D_{uu}/u_*^2 measured at different heights when plotted against $r/\kappa z$ (Fig. 14a)

and r/l_ϵ (Fig. 14b) for each experiment. The ensemble averages (across all data runs; see Table 1) of the profile of $P/\epsilon \approx l_\epsilon/\kappa z$ are also shown as insets to the figure. In Fig. 14a, it is clear that the inertial length scale κz does not collapse D_{uu}/u_*^2 at different heights, especially in the RSL of canopy experiments (AMA and MAI) where P/ϵ deviates appreciably from unity. However, at a given height in each experiment (indicated by a single color; e.g., red color for $z/h = 1$ in AMA experiment), the structure functions from different realizations/runs fall onto a single curve, indicating that normalization by u_*^2 (different across runs) collapses D_{uu} at the same height. Note that the LAKE data may suffer from wave effects that lead to some nonstationary effects (noticeable in Fig. 14). In contrast, the length scale l_ϵ performs much better in collapsing the height-dependent D_{uu}/u_*^2 in both the RSL and ASL (cf. Figs. 14a and 14b), albeit there are small departures at large r . Since $l_\epsilon/\kappa z > 1$ very close to the surface (or d_0) and approaches unity with increasing height, the effect of l_ϵ on shifting the structure functions is more pronounced at lower heights. For instance, the extent of D_{uu}/u_*^2 in the region $r/l_\epsilon < 1$ (vertical black line in Fig. 14b) is wider by at least half a decade than its $r/\kappa z < 1$ counterpart (Fig. 14a), indicating that, as opposed to κz , l_ϵ shifts D_{uu}/u_*^2 to the left (more so for lower

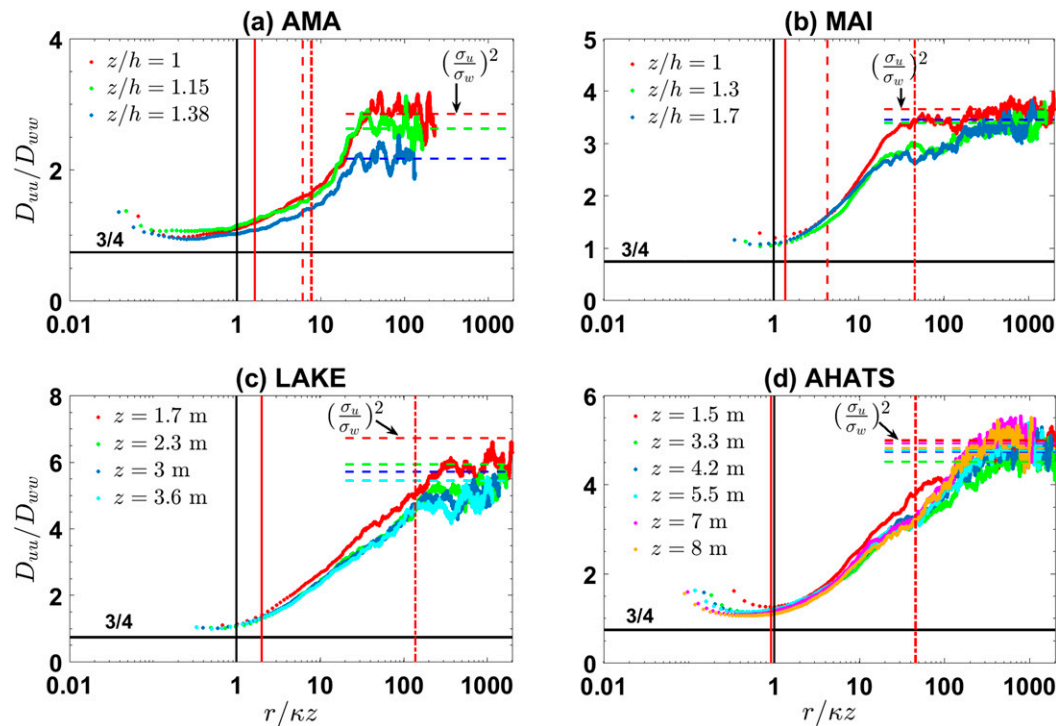


FIG. 13. Ratio of the structure functions D_{uu}/D_{ww} plotted against $r/\kappa z$ at each measurement height on a log-linear scale. As in Fig. 12, the length scales l_e , l_s , and L_u are shown as solid, dashed, and dash-dotted red lines, respectively. The horizontal dashed lines represent the ratio $D_{uu}/D_{ww} = (\sigma_u/\sigma_w)^2$ (calculated from the data) expected at the very large scales, while black horizontal lines correspond to $D_{uu}/D_{ww} = 3/4$ in the isotropic range.

heights where l_e is larger) to bring all the curves together. A similar conclusion can be made for the vertical velocity structure function D_{ww}/u_*^2 (shown in Fig. 15), where by comparing Figs. 15a and 15b, the experimental data can be seen to collapse better when normalizing r by l_e . To this end, Fig. 16 compares the performance of l_e with the shear length scale l_s (constant with height) in collapsing D_{uu}/u_*^2 for the canopy experiments only. While l_s appears to perform better than κz in the RSL (see Fig. 14), the dissipation length scale l_e remains a better similarity coordinate, indicating that the imbalance between local production and dissipation of TKE is the main mechanism of deviations from the classical z scaling.

5. Conclusions

This paper examined the classical arguments of Townsend's "attached" eddy model for the larger-than-inertial coherent motion in near-surface atmospheric flows. In particular, the scaling laws, phenomenology, and similarity of these attached anisotropic eddies are explored in the near-neutral roughness sublayer (RSL) above dense vegetation canopies and in the atmospheric

surface layer (ASL) over a short-grass field and a lake. As opposed to canonical turbulent boundary layers, where in the intermediate/inertial region the distance from the wall z is the similarity length scale, the focus was on the importance of additional similarity scales that emerge in near-surface atmospheric flows.

In the inertial layer, the large anisotropic scales of motion are known to exhibit a k^{-1} power law in the spectrum of the longitudinal velocity $E_{uu}(k)$ at moderately low wavenumbers k , typically at $kz < 1$, or alternatively a logarithmic scaling in the corresponding structure function $D_{uu}(r) \sim \ln(r)$ at large separation distances $r > z$. It was shown in prior studies that the crossover from the aforementioned large scales to inertial subrange scales is rather narrow and reasonably delineated by z . This z scaling was examined here in the RSL and ASL when production and dissipation of turbulence kinetic energy are not in local balance, leading to additional length scales such as the dissipation ($l_e = u_*^3/\epsilon$) length scale and the mixing/shear [$l_s = U(dU/dz)^{-1}$] length scale in the case of canopies. Five experiments (four atmospheric flows and one open-channel experiment), with multiple heights and multiple realizations/runs each, were used here to explore these

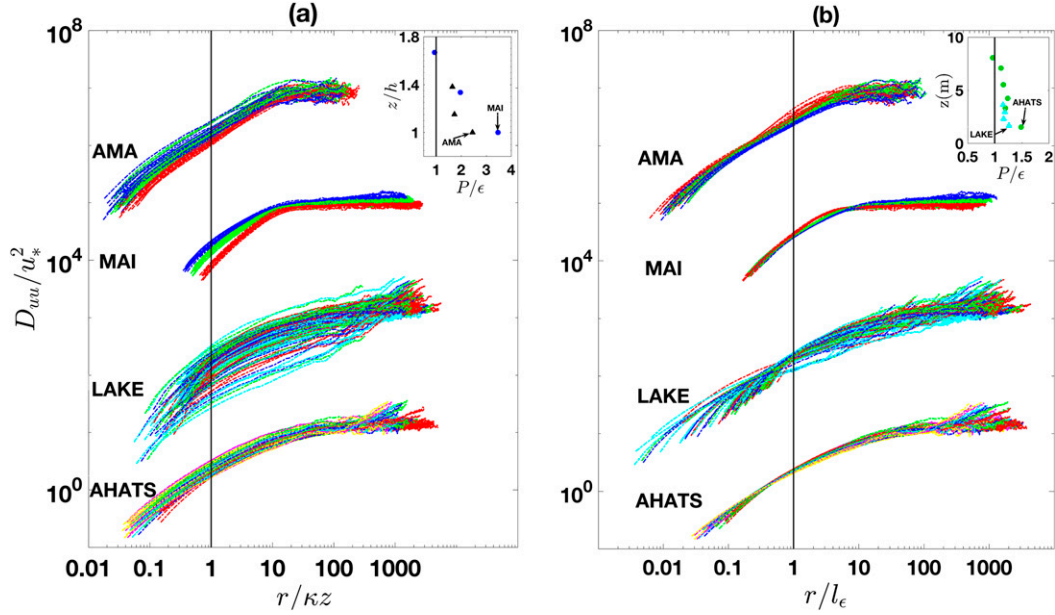


FIG. 14. Log-log plots of the normalized structure functions D_{uu}/u_*^2 at all measurement heights and all realizations/runs plotted against (a) r/kz and (b) r/l_ϵ . See Table 1 for the number of data runs and measurement heights at each site. The color code is such that red, blue, green, cyan, magenta, and yellow represent, respectively, increasing heights at each site. Plots are shifted vertically by two decades (except AHATS) for clarity. (inset) Vertical profiles of the ratio P/ϵ , with circle symbols in (a) and (b) indicating the MAI canopy and AHATS experiments, respectively, and triangle symbols in (a) and (b) indicating the AMA canopy and LAKE experiments, respectively.

aspects. The findings indicate that both k^{-1} in E_{uu} and/or $\ln(r)$ in D_{uu} exist within the RSL, ASL, and canonical turbulent boundary layers, although the extent of this range varies across experiments, with the RSL

exhibiting shorter extent because of the small separation of scales (the integral length scale is smaller than its ASL counterpart). Conversely, these scaling laws are absent in E_{ww} or D_{ww} for the vertical velocity

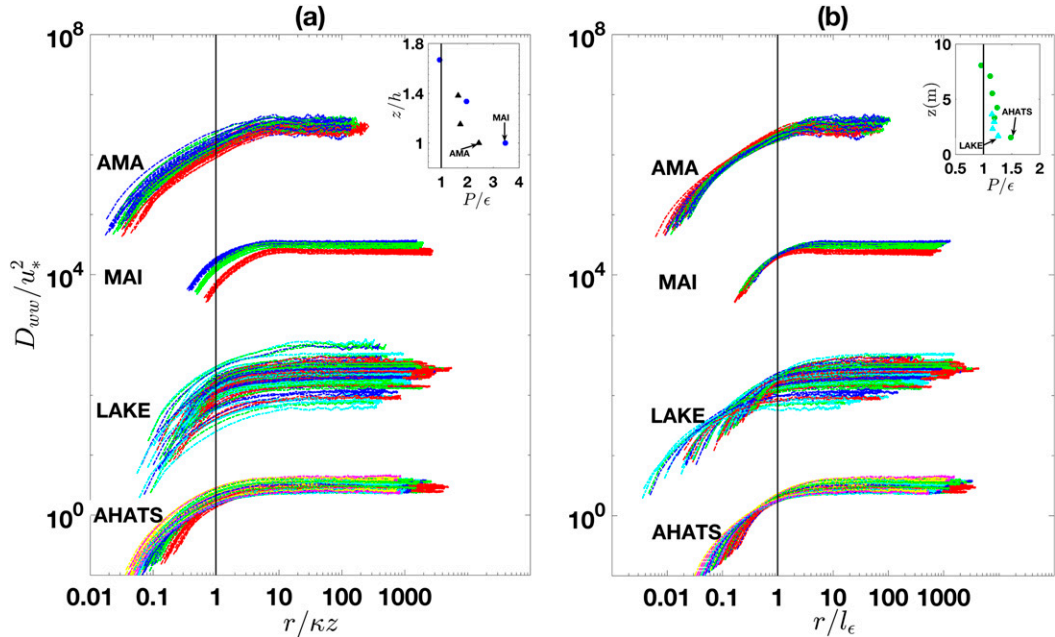


FIG. 15. As in Fig. 14, but for D_{wv}/u_*^2 .

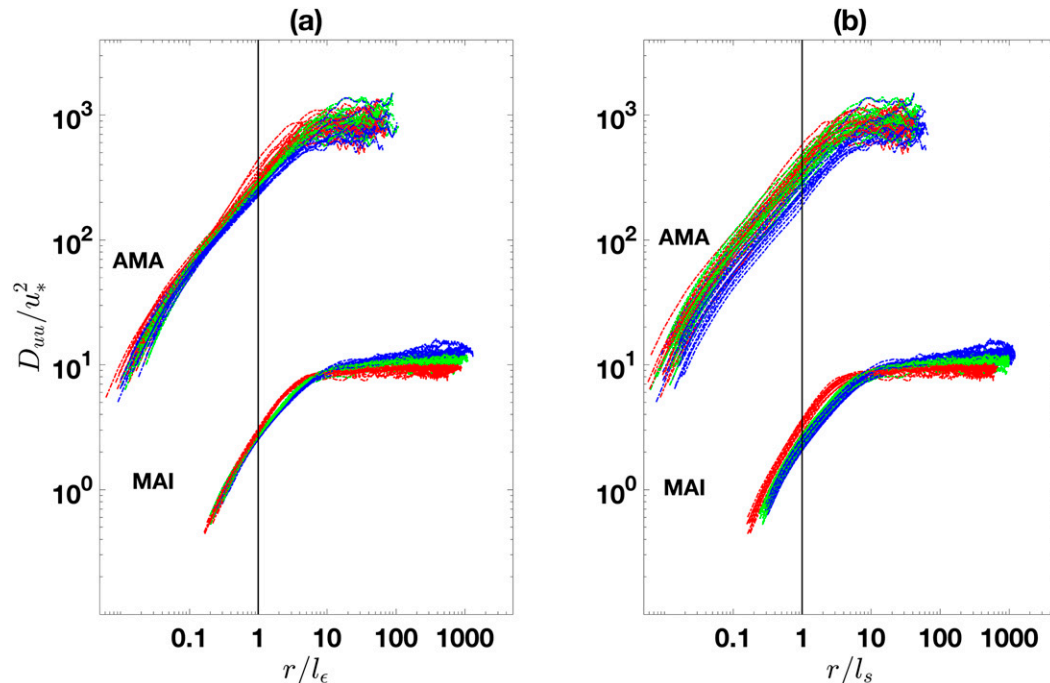


FIG. 16. Log-log plots of the normalized structure functions D_{uu}/u_*^2 at all available measurement heights and data runs for the canopy experiments only, plotted against (a) r/l_ϵ , and (b) r/l_s .

components except at large distances from the wall, where a short extent of a k^{-1} regime in E_{ww} or $\ln(r)$ in D_{ww} emerges.

Phenomenological aspects of the coherent eddies reveal that the statistics of velocity increments Δu and Δw approach a Gaussian-like behavior at large r . These findings are in broad agreement with the accepted picture of canonical turbulent boundary layers. Eddies associated with these large anisotropic scales are shown to be further responsible for momentum/energy production corroborated by large positive (negative) excursions in Δu accompanied by negative (positive) ones in Δw . In terms of similarity, normalizing the separation distance r by the inertial length scale κz did not collapse the structure functions D_{uu} and D_{ww} at different heights within the RSL and ASL, defying therefore the classical z -scaling picture in this context of imbalance between local TKE production and dissipation. The length scale $l_\epsilon = u_*^3/\epsilon$ shows an improved performance in collapsing these structure functions at different heights in both the RSL and ASL, owing to the fact that l_ϵ accounts for the aforementioned energy imbalance. Despite the difficulty in accurately estimating l_ϵ from experimental data, this scale represents a theoretical alternative to the z scaling in wall-bounded flows up to heights where it converges to the inertial scale κz .

Acknowledgments. Ghannam and Katul acknowledge support from the National Science Foundation

(NSF-CBET-103347 and NSF-EAR-1344703), the U.S. Department of Energy (DOE) through the office of Biological and Environmental Research (BER) Terrestrial Ecosystem Science (TES) Program (DE-SC0006967 and DE-SC0011461), and the Duke University WISENet Program sponsored by the National Science Foundation (Grant DGE-1068871). Bou-Zeid acknowledges support from the Princeton Environmental Institute's Climate and Energy Grand Challenge Program. The authors acknowledge Professor Marc Parlange and the team of Environmental Fluid Mechanics and Hydrology Laboratory at the École Polytechnique Fédérale de Lausanne for sharing the lake data. The AHATS data were collected by NCAR Integrated Surface Flux Facility. The authors would like to acknowledge operational, technical, and scientific support provided by NCAR Earth Observing Laboratory, sponsored by the National Science Foundation.

REFERENCES

- Anselmetti, F., Y. Gagne, E. Hopfinger, and R. Antonia, 1984: High-order velocity structure functions in turbulent shear flows. *J. Fluid Mech.*, **140**, 63–89, <https://doi.org/10.1017/S0022112084000513>.
- Balakumar, B. J., and R. J. Adrian, 2007: Large- and very-large-scale motions in channel and boundary-layer flows. *Philos. Trans. Roy. Soc. London*, **365A**, 665–681, <https://doi.org/10.1098/rsta.2006.1940>.

- Banerjee, T., and G. G. Katul, 2013: Logarithmic scaling in the longitudinal velocity variance explained by a spectral budget. *Phys. Fluids*, **25**, 125106, <https://doi.org/10.1063/1.4837876>.
- , —, S. Salesky, and M. Chamecki, 2015: Revisiting the formulations for the longitudinal velocity variance in the unstable atmospheric surface layer. *Quart. J. Roy. Meteor. Soc.*, **141**, 1699–1711, <https://doi.org/10.1002/qj.2472>.
- Bou-Zeid, E., N. Vercauteren, M. B. Parlange, and C. Meneveau, 2008: Scale dependence of subgrid-scale model coefficients: An a priori study. *Phys. Fluids*, **20**, 115 106, <https://doi.org/10.1063/1.2992192>.
- Busch, N. E., and H. A. Panofsky, 1968: Recent spectra of atmospheric turbulence. *Quart. J. Roy. Meteor. Soc.*, **94**, 132–148, <https://doi.org/10.1002/qj.49709440003>.
- Chamecki, M., 2013: Persistence of velocity fluctuations in non-Gaussian turbulence within and above plant canopies. *Phys. Fluids*, **25**, 115110, <https://doi.org/10.1063/1.4832955>.
- , and N. L. Dias, 2004: The local isotropy hypothesis and the turbulent kinetic energy dissipation rate in the atmospheric surface layer. *Quart. J. Roy. Meteor. Soc.*, **130**, 2733–2752, <https://doi.org/10.1256/qj.03.155>.
- , —, S. T. Salesky, and Y. Pan, 2017: Scaling laws for the longitudinal structure function in the atmospheric surface layer. *J. Atmos. Sci.*, **74**, 1127–1147, <https://doi.org/10.1175/JAS-D-16-0228.1>.
- Charuchittipan, D., and J. D. Wilson, 2009: Turbulent kinetic energy dissipation in the surface layer. *Bound.-Layer Meteor.*, **132**, 193–204, <https://doi.org/10.1007/s10546-009-9399-x>.
- Chung, D., I. Marusic, J. Monty, M. Vallikivi, and A. Smits, 2015: On the universality of inertial energy in the log layer of turbulent boundary layer and pipe flows. *Exp. Fluids*, **56**, 141, <https://doi.org/10.1007/s00348-015-1994-7>.
- Davidson, P., and P.-Å. Krogstad, 2009: A simple model for the streamwise fluctuations in the log-law region of a boundary layer. *Phys. Fluids*, **21**, 055105, <https://doi.org/10.1063/1.3140075>.
- , and —, 2014: A universal scaling for low-order structure functions in the log-law region of smooth- and rough-wall boundary layers. *J. Fluid Mech.*, **752**, 140–156, <https://doi.org/10.1017/jfm.2014.286>.
- , T. Nickels, and P.-Å. Krogstad, 2006: The logarithmic structure function law in wall-layer turbulence. *J. Fluid Mech.*, **550**, 51–60, <https://doi.org/10.1017/S0022112005008001>.
- Del Álamo, J. C., J. Jiménez, P. Zandonade, and R. D. Moser, 2004: Scaling of the energy spectra of turbulent channels. *J. Fluid Mech.*, **500**, 135–144, <https://doi.org/10.1017/S002211200300733X>.
- de Silva, C., I. Marusic, J. Woodcock, and C. Meneveau, 2015: Scaling of second- and higher-order structure functions in turbulent boundary layers. *J. Fluid Mech.*, **769**, 654–686, <https://doi.org/10.1017/jfm.2015.122>.
- Drobninski, P., P. Carloti, R. K. Newsom, R. M. Banta, R. C. Foster, and J.-L. Redelsperger, 2004: The structure of the near-neutral atmospheric surface layer. *J. Atmos. Sci.*, **61**, 699–714, [https://doi.org/10.1175/1520-0469\(2004\)061<0699:TSOTNA>2.0.CO;2](https://doi.org/10.1175/1520-0469(2004)061<0699:TSOTNA>2.0.CO;2).
- , —, J.-L. Redelsperger, V. Masson, R. M. Banta, and R. K. Newsom, 2007: Numerical and experimental investigation of the neutral atmospheric surface layer. *J. Atmos. Sci.*, **64**, 137–156, <https://doi.org/10.1175/JAS3831.1>.
- Finnigan, J., 2000: Turbulence in plant canopies. *Annu. Rev. Fluid Mech.*, **32**, 519–571, <https://doi.org/10.1146/annurev.fluid.32.1.519>.
- Freire, L. S., and Coauthors, 2017: Turbulent mixing and removal of ozone within an Amazon rainforest canopy. *J. Geophys. Res. Atmos.*, **122**, 2791–2811, <https://doi.org/10.1002/2016JD026009>.
- Fuentes, J. D., and Coauthors, 2016: Linking meteorology, turbulence, and air chemistry in the Amazon rain forest. *Bull. Amer. Meteor. Soc.*, **97**, 2329–2342, <https://doi.org/10.1175/BAMS-D-15-00152.1>.
- Gerken, T., and Coauthors, 2018: Investigating the mechanisms responsible for the lack of surface energy balance closure in a central Amazonian tropical rainforest. *Agric. For. Meteorol.*, <https://doi.org/10.1016/j.agrformet.2017.03.023>, in press.
- Ghannam, K., T. Duman, S. T. Salesky, M. Chamecki, and G. Katul, 2017: The non-local character of turbulence asymmetry in the convective atmospheric boundary layer. *Quart. J. Roy. Meteor. Soc.*, **143**, 494–507, <https://doi.org/10.1002/qj.2937>.
- Gleicher, S. C., M. Chamecki, S. A. Isard, Y. Pan, and G. G. Katul, 2014: Interpreting three-dimensional spore concentration measurements and escape fraction in a crop canopy using a coupled Eulerian–Lagrangian stochastic model. *Agric. For. Meteorol.*, **194**, 118–131, <https://doi.org/10.1016/j.agrformet.2014.03.020>.
- Guala, M., M. Metzger, and B. J. McKeon, 2011: Interactions within the turbulent boundary layer at high Reynolds number. *J. Fluid Mech.*, **666**, 573–604, <https://doi.org/10.1017/S0022112010004544>.
- Högström, U., J. Hunt, and A.-S. Smedman, 2002: Theory and measurements for turbulence spectra and variances in the atmospheric neutral surface layer. *Bound.-Layer Meteorol.*, **103**, 101–124, <https://doi.org/10.1023/A:1014579828712>.
- Hsieh, C.-I., and G. G. Katul, 1997: Dissipation methods, Taylor’s hypothesis, and stability correction functions in the atmospheric surface layer. *J. Geophys. Res.*, **102**, 16 391–16 405, <https://doi.org/10.1029/97JD00200>.
- Hunt, J., and P. Carloti, 2001: Statistical structure at the wall of the high Reynolds number turbulent boundary layer. *Flow Turbul. Combust.*, **66**, 453–475, <https://doi.org/10.1023/A:1013519021030>.
- Hutchins, N., K. Chauhan, I. Marusic, J. Monty, and J. Klewicki, 2012: Towards reconciling the large-scale structure of turbulent boundary layers in the atmosphere and laboratory. *Bound.-Layer Meteorol.*, **145**, 273–306, <https://doi.org/10.1007/s10546-012-9735-4>.
- Jiménez, J., 2012: Cascades in wall-bounded turbulence. *Annu. Rev. Fluid Mech.*, **44**, 27–45, <https://doi.org/10.1146/annurev-fluid-120710-101039>.
- Kaimal, J. C., J. C. Wyngaard, Y. Izumi, and O. R. Coté, 1972: Spectral characteristics of surface-layer turbulence. *Quart. J. Roy. Meteor. Soc.*, **98**, 563–589, <https://doi.org/10.1002/qj.49709841707>.
- Katul, G., and C.-R. Chu, 1998: A theoretical and experimental investigation of energy-containing scales in the dynamic sub-layer of boundary-layer flows. *Bound.-Layer Meteorol.*, **86**, 279–312, <https://doi.org/10.1023/A:1000657014845>.
- , C.-I. Hsieh, and J. Sigmon, 1997: Energy-inertial scale interactions for velocity and temperature in the unstable atmospheric surface layer. *Bound.-Layer Meteorol.*, **82**, 49–80, <https://doi.org/10.1023/A:1000178707511>.
- , A. Porporato, and V. Nikora, 2012: Existence of k^{-1} power-law scaling in the equilibrium regions of wall-bounded turbulence explained by Heisenberg’s eddy viscosity. *Phys. Rev.*, **86E**, 066311, <https://doi.org/10.1103/PhysRevE.86.066311>.

- , C. Manes, A. Porporato, E. Bou-Zeid, and M. Chamecki, 2015: Bottlenecks in turbulent kinetic energy spectra predicted from structure function inflections using the von Kármán-Howarth equation. *Phys. Rev.*, **92E**, 033009, <https://doi.org/10.1103/PhysRevE.92.033009>.
- , T. Banerjee, D. Cava, M. Germano, and A. Porporato, 2016: Generalized logarithmic scaling for high-order moments of the longitudinal velocity component explained by the random sweeping decorrelation hypothesis. *Phys. Fluids*, **28**, 095104, <https://doi.org/10.1063/1.4961963>.
- Kolmogorov, A. N., 1941: The local structure of turbulence in incompressible viscous fluid for very large Reynolds numbers. *Dokl. Akad. Nauk SSSR*, **30**, 299–303.
- Kunkel, G. J., and I. Marusic, 2006: Study of the near-wall-turbulent region of the high-Reynolds-number boundary layer using an atmospheric flow. *J. Fluid Mech.*, **548**, 375–402, <https://doi.org/10.1017/S0022112005007780>.
- Li, D., G. G. Katul, and P. Gentile, 2016: The k^{-1} scaling of air temperature spectra in atmospheric surface layer flows. *Quart. J. Roy. Meteor. Soc.*, **142**, 496–505, <https://doi.org/10.1002/qj.2668>.
- Marusic, I., B. J. McKeon, P. A. Monkewitz, H. M. Nagib, A. J. Smits, and K. R. Sreenivasan, 2010: Wall-bounded turbulent flows at high Reynolds numbers: Recent advances and key issues. *Phys. Fluids*, **22**, 065103, <https://doi.org/10.1063/1.3453711>.
- , J. P. Monty, M. Hultmark, and A. J. Smits, 2013: On the logarithmic region in wall turbulence. *J. Fluid Mech.*, **716**, R3, <https://doi.org/10.1017/jfm.2012.511>.
- Meneveau, C., and I. Marusic, 2013: Generalized logarithmic law for high-order moments in turbulent boundary layers. *J. Fluid Mech.*, **719**, R1, <https://doi.org/10.1017/jfm.2013.61>.
- Metzger, M. M., and J. C. Klewicki, 2001: A comparative study of near-wall turbulence in high and low Reynolds number boundary layers. *Phys. Fluids*, **13**, 692–701, <https://doi.org/10.1063/1.1344894>.
- Monin, A., and A. M. Yaglom, 1975: *Statistical Fluid Mechanics: Mechanics of Turbulence*. Vol. 2. MIT Press, 874 pp.
- Nikora, V., 1999: Origin of the “ -1 ” spectral law in wall-bounded turbulence. *Phys. Rev. Lett.*, **83**, 734–736, <https://doi.org/10.1103/PhysRevLett.83.734>.
- Obukhov, A., 1949: The local structure of atmospheric turbulence. *Dokl. Akad. Nauk SSSR*, **67**, 643–646.
- Pan, Y., and M. Chamecki, 2016: A scaling law for the shear-production range of second-order structure functions. *J. Fluid Mech.*, **801**, 459–474, <https://doi.org/10.1017/jfm.2016.427>.
- , —, and H. M. Nepf, 2016: Estimating the instantaneous drag–wind relationship for a horizontally homogeneous canopy. *Bound.-Layer Meteor.*, **160**, 63–82, <https://doi.org/10.1007/s10546-016-0137-x>.
- Perry, A., and C. Abell, 1977: Asymptotic similarity of turbulence structures in smooth- and rough-walled pipes. *J. Fluid Mech.*, **79**, 785–799, <https://doi.org/10.1017/S0022112077000457>.
- , S. Henbest, and M. Chong, 1986: A theoretical and experimental study of wall turbulence. *J. Fluid Mech.*, **165**, 163–199, <https://doi.org/10.1017/S002211208600304X>.
- Poggi, D., A. Porporato, L. Ridolfi, J. Albertson, and G. Katul, 2004: The effect of vegetation density on canopy sub-layer turbulence. *Bound.-Layer Meteor.*, **111**, 565–587, <https://doi.org/10.1023/B:BOUN.0000016576.05621.73>.
- Prandtl, L., 1925: Bericht über untersuchungen zur ausgebildeten turbulenz. *Z. Angew. Math. Mech.*, **5**, 136–139.
- Raupach, M. R., J. J. Finnigan, and Y. Brunet, 1996: Coherent eddies and turbulence in vegetation canopies: The mixing-layer analogy. *Bound.-Layer Meteor.*, **78**, 351–382, <https://doi.org/10.1007/BF00120941>.
- Salesky, S. T., and M. Chamecki, 2012: Random errors in turbulence measurements in the atmospheric surface layer: Implications for Monin–Obukhov similarity theory. *J. Atmos. Sci.*, **69**, 3700–3714, <https://doi.org/10.1175/JAS-D-12-096.1>.
- , —, and E. Bou-Zeid, 2017: On the nature of the transition between roll and cellular organization in the convective boundary layer. *Bound.-Layer Meteor.*, **163**, 41–68, <https://doi.org/10.1007/s10546-016-0220-3>.
- Sreenivasan, K. R., and R. Antonia, 1997: The phenomenology of small-scale turbulence. *Annu. Rev. Fluid Mech.*, **29**, 435–472, <https://doi.org/10.1146/annurev.fluid.29.1.435>.
- Stevens, R. J., M. Wilczek, and C. Meneveau, 2014: Large-eddy simulation study of the logarithmic law for second- and higher-order moments in turbulent wall-bounded flow. *J. Fluid Mech.*, **757**, 888–907, <https://doi.org/10.1017/jfm.2014.510>.
- Taylor, G. I., 1938: The spectrum of turbulence. *Proc. Roy. Soc. London*, **164A**, 476–490, <https://doi.org/10.1098/rspa.1938.0032>.
- Tchen, C.-M., 1953: On the spectrum of energy in turbulent shear flow. *J. Res. Natl. Bur. Stand. (U.S.)*, **50**, 51–62, <https://doi.org/10.6028/jres.050.009>.
- Townsend, A. A., 1961: Equilibrium layers and wall turbulence. *J. Fluid Mech.*, **11**, 97–120, <https://doi.org/10.1017/S0022112061000883>.
- , 1976: *The Structure of Turbulent Shear Flow*. Cambridge University Press, 429 pp.
- UCAR–NCAR Earth Observing Laboratory, 1990: Integrated Surface Flux System. NCAR Earth Observing Laboratory, accessed 15 January 2017, <https://doi.org/10.5065/D6ZC80XJ>.
- Vallikivi, M., B. Ganapathisubramani, and A. Smits, 2015: Spectral scaling in boundary layers and pipes at very high Reynolds numbers. *J. Fluid Mech.*, **771**, 303–326, <https://doi.org/10.1017/jfm.2015.181>.
- Vercauteren, N., E. Bou-Zeid, M. B. Parlange, U. Lemmin, H. Huwald, J. Selker, and C. Meneveau, 2008: Subgrid-scale dynamics of water vapour, heat, and momentum over a lake. *Bound.-Layer Meteor.*, **128**, 205–228, <https://doi.org/10.1007/s10546-008-9287-9>.
- von Kármán, T., 1930: Mechanische Ähnlichkeit und turbulenz. *Nachr. Ges. Wiss. Göttingen Math.-Phys. Kl.*, **68**, 58–76.
- , and L. Howarth, 1938: On the statistical theory of isotropic turbulence. *Proc. Roy. Soc. London*, **164A**, 192–215, <https://doi.org/10.1098/rspa.1938.0013>.
- Wyngaard, J. C., and S. F. Clifford, 1977: Taylor’s hypothesis and high-frequency turbulence spectra. *J. Atmos. Sci.*, **34**, 922–929, [https://doi.org/10.1175/1520-0469\(1977\)034<0922:THAHTS>2.0.CO;2](https://doi.org/10.1175/1520-0469(1977)034<0922:THAHTS>2.0.CO;2).